

New Efficient Detector for Radiation Therapy Imaging using Gas Electron Multipliers

Janina Östling



Department of Medical Radiation Physics
Karolinska Institutet & Stockholm University 2006



New Efficient Detector for Radiation Therapy Imaging
using Gas Electron Multipliers

Doctoral Thesis, Stockholm, 2006

*Medical Radiation Physics Department,
Stockholm University & Karolinska Institutet*

All previously published papers were reproduced with permission from the publisher.

Printed in Sweden by Universitetservice US-AB, Stockholm, 2006
©Janina Östling 2006 (pp 1-49)
ISBN 91-7155-218-9

Abstract

Currently film is being replaced by electronic detectors for portal imaging in radiation therapy. This development offers obvious advantages such as on-line quality assurance and digital images that can easily be accessed, processed and communicated. In spite of the improvements, the image quality has not been significantly enhanced, partly since the quantum efficiency compared to film is essentially the same, and the new electronic devices also suffer from sensitivity to the harsh radiation environment. In this thesis we propose a third generation electronic portal imaging device with increased quantum efficiency and potentially higher image quality. Due to the parallel readout capability it is much faster than current devices, providing at least 200 frames per second (fps), and would even allow for a quality assurance and adaptive actions after each accelerator pulse. The new detector is also sensitive over a broader range of energies (10 keV - 50 MeV) and can be used to obtain diagnostic images immediately prior to the treatment without repositioning the patient. The imaging could be in the form of portal imaging or computed tomography. The new detector is based on a sandwich design containing several layers of Gas Electron Multipliers (GEMs) in combination with, or integrated with, perforated converter plates. The charge created by the ionizing radiation is drifted to the bottom of the assembly where a tailored readout system collects and digitizes the charge. The new readout system is further designed in such a way that no sensitive electronics is placed in the radiation beam and the detector is expected to be radiation resistant since it consists mainly of kapton, copper and gas.

A single GEM detector was responding linearly when tested with a 50 MV photon beam at a fluence rate of $\sim 10^{10}$ photons $\text{mm}^{-2}\text{s}^{-1}$ during 3-5 μs long pulses, but also with x-ray energies of 10-50 keV at a fluence rate of up to $\sim 10^8$ photons $\text{mm}^{-2}\text{s}^{-1}$. The electron transmission of a 100 μm thick Cu plate with an optical transparency of $\sim 46\%$ was found to be $\sim 15.4\%$, i.e. the effective hole transmission for the electrons was about one third of the hole area. A low effective GEM gain is enough to compensate for the losses in converters of this dimension. A prototype for the dedicated electronic readout system was designed with 50×100 pixels at a pitch of $1.27 \text{ mm} \times 1.27 \text{ mm}$. X-ray images were achieved with a single GEM layer and also in a double GEM setup with a converter plate interleaved. To verify the readout speed a Newton pendulum was imaged at a frame rate of 70 fps and alpha particles were imaged in 188 fps. The experimental studies indicates that the existing prototype can be developed as a competitive alternative for imaging in radiation therapy.

List of papers

This thesis is based on the following papers which will be referred to by their Roman numerals:

I. J. Ostling, A. Brahme, M. Danielsson, C. Iacobaeus, V. Peskov, "Amplification and conditioning properties of GEM and CAT detector for beam monitoring", Proceedings of Intern. Workshop on Micro Pattern Gaseous Detectors 1999, Orsay, France (1999)

II. A. Brahme, M. Danielsson, C. Iacobaeus, J. Ostling, V. Peskov, M. Wallmark, "Evaluation of a GEM and CAT-based detector for radiation therapy beam monitoring", Nucl. Instr. and Meth. in Physics Research A, 454 (2000) 136-141

III. C. Iacobaeus, A. Brahme, M. Danielsson, P. Fonte, J. Ostling, V. Peskov, M. Wallmark, "A novel portal imaging device for advanced radiation therapy", IEEE T NUCL SCI 48 (4): 1496-1502 Part 2 AUG 2001

IV. J. Ostling, A. Brahme, M. Danielsson, T. Francke, C. Iacobaeus, V. Peskov, "Study of hole-type gas multiplication structures for portal imaging and other high counting rate applications", IEEE T NUCL SCI 50 (4): 809-819 Part 1 AUG 2003

V. J. Östling, A. Brahme, M. Danielsson, C. Iacobaeus and V. Peskov, "A radiation tolerant electronic readout system for portal imaging", Nucl. Instr. and Meth. in Physics Research A, 525 (2004) 308-312

References [1]-[7] are other papers by the author but not directly included in the present thesis.

Contents

Abstract	iii
List of included publications	iv
Table of contents	vi
1 Introduction	1
1.1 Clinical background	1
1.2 Existing portal imaging systems	2
1.3 On board Computed Tomography	3
1.4 Brief summary of the state of the art for portal imaging	4
2 Design of the new imaging system	5
2.1 Detector components	5
2.1.1 The Gas Electron Multiplier	7
2.1.2 Gas mixture considerations	9
2.1.3 Metal conversion layer for high energy photons	10
2.1.4 Electronic readout system	11
2.2 Estimation of achievable detector efficiency	12
3 Experimental realization	22

3.1	Materials	22
3.1.1	Diagnostic x-ray beam (~ 50 kV)	22
3.1.2	Therapeutic Racetrack microtron beam (~ 50 MV)	23
3.1.3	Test chambers	24
3.1.4	High voltage supplies	24
3.1.5	Experimental procedures	25
3.2	Experimental results	26
3.2.1	Data acquisition system	26
3.2.2	GEM measurements	28
3.2.3	Double GEM + metal converter plate setup	32
4	Discussion and conclusions	38
4.1	Potential clinical applications	38
4.2	Summary of the experimental work	39
4.3	Future developments	41
4.4	Concluding advantages and challenges with the new detector	42
	Acknowledgements	43
	Abbreviations	45
	References	45

Chapter 1

Introduction

1.1 Clinical background

In modern radiation therapy intensity modulated dose delivery is used to maximize the probability of achieving complication free tumor cure. Accurate alignment of the patient with respect to the therapeutic beam is of major importance. The classical way of photon beam portal verification is portal imaging of the beam transmitted through the patient. This allows accurate verification of the position of the collimated intensity modulated therapy beam in relation to normal tissue and bony anatomy as visualized by transmission imaging. Portal imaging therefore could allow readjustment of the relative positions of the edge of the incoming beam and the patient, and may even enable adjustment of the intensity modulation by adaptive radiation therapy. In radiation therapy there is always a risk for internal tumor motion from one day to the next during the course of the treatment. For all targets internal margins have to be included during the treatment planning. To account for uncertainties in the patient setup in relation to the therapeutic beam, a setup margin is added to the therapeutic beam to account for uncertainties in beam patient alignment to safely cover the tumor, despite setup uncertainties [8]. A consequence of this strategy is that the dose might have to be reduced in order not to harm healthy tissues that are located inside the target volume. However, using intensity modulated radiation therapy, IMRT, for a given internal margin the tumor cure can successively be improved [8], not least by adaptive approaches [9]. For decades the MV portal imaging by film has been used on a weekly basis, and with the development of modern electronic portal imaging devices, EPIDs, in recent years it has become possible to control the treatment on a daily basis. Another development is to include on board computed tomography, CT, with a therapeutic or diagnostic x-ray source. When the tumor position is known more accurately prior to the treatment, the safety margin can be reduced and the dose to the tumor increased, resulting in an improved treatment outcome for the patient.

1.2 Existing portal imaging systems

The radiation treatment is delivered with an electron accelerator operated at a maximum accelerating potential ranging from 2-50 MV. Informative review articles about electronic portal imaging devices has been published quite recently, e.g. [10] and [11]. All commercial portal imaging systems use a single metal plate for the x-ray conversion and while $\sim 4\%$ of the incident photons interact in the converter, less than 1% will contribute to the detector signal when irradiated by a 2 MeV x-ray beam [11].

Portal film

The classical way to obtain portal images is to use MV portal films. The film development is time consuming and it cannot be evaluated in real time, it only allows for on-line corrections on a 5-10 minutes or longer time scale, e.g. using adaptive therapy [9]. Further, the film requires a handling procedure and a non negligible effort when placing each film, developing it and archiving it. It should also be mentioned that the response of the film is non-linear with dose.

Liquid ionization chambers

The ionization chamber is an old and well known type of detector. Also in this case an additional metal plate, used as a build up layer, is placed in front of the detector. The idea of using a liquid substance as detecting medium rather than gas, enhances the interaction cross section due to the increased density and higher charge production. The liquid ionization chamber marketed by Varian Medical Systems, the PortalVision LC250TM, uses a scanned readout method and it requires approximately 3 seconds to achieve one image in standard mode and 0.95 seconds in fast mode [12].

Scintillating screen & CCD based systems

A screen made of phosphorous or crystalline material is emitting visible light when being hit by the electrons released by the therapy photons interacting in the build up layer placed in front of the screen. The light is reflected by a mirror and directed to a CCD or a video camera, as was used already in the 1960's [13]. The cameras can not survive a long time in the beam, therefore the photons are reflected in 45° in the mirror directed to the camera, which thus may be placed outside the beam region. Unfortunately this makes the system rather bulky and inconvenient in a treatment room. The photons are emitted in all angles from the phosphor screen, but only those emitted in a small cone subtended by the lens of the camera, contributes to the signal, and this is only 0.1-0.01% [11]. The demagnification is thus a substantial quantum sink.

As an example a stand alone portal imager, PORTproTM, based on a CCD readout has been developed by the Israelian company ELIAV [14]. The total height of the system is 190 cm and the weight 65 kg. It is not attached to the gantry and can not provide images through out the rotation. TheraViewTM is a video camera based system that is delivered by Cablon Medical [15]. The

scintillator has an area of $40\text{ cm} \times 40\text{ cm}$ and the detector pixels are 0.78 mm squared. In the treatment sequence mode the readout speed is up to one image per second according to specifications.

Active Matrix Flat Panel Imager (AMFPI)

The latest development of the scintillating screen based systems, and also the most popular EPID today, is the active matrix flat panel imager. In addition to the metal plate, the impinging x-ray can interact directly in the phosphor layer and the photon detectors and a total of $\sim 2\%$ of the incident radiation (including interactions in the build up layer) contributes to the detector signal in current AMFPI EPIDs [16]. With an increasing thickness of the screen the spatial resolution gets worse however [11]. The emitted visible light from the phosphor screen is absorbed by photodiodes made of amorphous silicon at the readout plate. Each photodiode is connected to its own thin film transistor, placed in an immediate vicinity of the amorphous silicon, which is routed to common lines for one row of pixels. The collected charge at each pixel is read out sequentially with one row at a time.

One example is the amorphous silicon detector XRD 1640 AN ES which is manufactured by Perkin Elmer. The active area is about $41\text{ cm} \times 41\text{ cm}$ with a pixel pitch of $400\text{ }\mu\text{m}$, and it provides live images at a speed of 15 fps. The maximum energy sensitivity ranges up to 15 MeV [17]. The company delivers flat panels to be integrated in the portal imaging systems sold by Elekta AB and Siemens AG, named iViewGTTM [18] and BeamViewTM [19] respectively. Varian Medical Systems has its own AMFPI detector named PortalVision aS500TM [22]. The active area of this device is $40\text{ cm} \times 30\text{ cm}$ with a pixel pitch of 0.784 mm , and the readout speed is 10 fps.

1.3 On board Computed Tomography

Diagnostic CT x-ray imaging typically employ an $80\text{-}140\text{ kV}$ spectrum [20]. The average x-ray energy is approximately one third of the maximum value which is approximately given by the kV setting of the high voltage generator of the x-ray tube.

The three major companies on the market for radiation therapy equipment have come up with separate solutions for how to combine EPID information with information from diagnostic imaging with a CT in the treatment position.

In Elekta SynergyTM [18] and Varian On-Board ImagerTM [22], an x-ray tube has been mounted on the gantry, placed orthogonally to the therapeutic beam and its portal imager. Opposite and in line with the diagnostic x-ray tube, a low energy sensitive flat panel detector has been mounted. The Varian flat panel detector is mounted on robotically controlled arms which operate along three axes, and can be retracted when not in use. The Elekta system is also attached to an extractable arm. Hence there are two separate imaging systems (Diagnostic

x-ray + CT, and Therapeutic beam + EPID) and two beam sources located around the patient in both systems described. This feature brings the possibility to reconstruct a cone beam CT volume of the patient at the treatment position immediately prior to the treatment as well as using it to verify the patient positioning.

These systems are able to track the tumor in real time, so called dynamic imaging, i.e. to catch intra-fraction tumor motions. A discussion about this possibility and a comparative study with a double setup of two kV detectors can be found in [21]. Note that in the latter case three detectors (2 CT + 1 EPID) and two extra x-ray sources are required in addition to the treatment accelerator.

Siemens ARTISTETM [19] has two imaging panels, one for a kV beam placed at the opening of the gantry head, and the other one for portal imaging located in the beam stopper. An x-ray source is situated behind the EPID to provide the beam for the low energy detector. The advantage with such a solution compared to the Elekta and Varian systems, is that it provides both entrance and exit treatment ports and a more compact design.

The new Tomotherapy system [23] has a completely enclosed cylindrical gantry, like a CT scanner, and uses only MV-imaging to obtain fast therapeutic CT images similar to earlier detector designs [24].

1.4 Brief summary of the state of the art for portal imaging

Existing EPIDs have several advantages over portal film. However, a drawback is the poor image quality due to the inherent very low quantum efficiency of the detectors. The best systems available, the AMFPIs, are limited to extract information from $\sim 2\%$ of the incident photon beam only [16]. To increase the detector efficiency one might think of using a thicker metal converter. However, the absorption of the primary electrons generated in the metal plate will then increase with the converter thickness giving minimal gain.

The work presented in this thesis address the possibilities to overcome the shortcoming of present EPID systems through a new multilayer detector technique. It will offer a higher detection efficiency, a substantial increase in the imaging frame rate, an improved radiation tolerance and the combination of a diagnostic and therapeutic x-ray detection in a single device.

Chapter 2

Design of the new imaging system

2.1 Detector components

General detector function

The multilayer detector was suggested by A. Brahme and M. Danielsson [25] paper [I-V], and the outline of the detector design is indicated in figure 2.1. It is a gaseous detector, hence all detector parts are included in a sealed chamber. Varying gas mixtures can be used and the gas is supplied at atmospheric pressure. As specified in the figure, photons are impinging at the top of the chamber through an entrance window. Low energy photons interact either in the gas volume of the drift region, or in the combined drift electrode/low-energy-converter. The converter plates shown in the illustration have the task to convert high energy photons to electrons. Further does the detector function require gas electron multipliers (GEMs) to be installed between every converter, and a pixelized readout plate.

Diagnostic energies

One can think of two strategies to detect x-rays with diagnostic energies. The first one is to use the gas itself as the converter, while the second is to use the drift electrode as a converter. If using the gas layer in the drift region as conversion medium, a gas with a high atomic number should be used. The photoelectric effect is the dominating photon interaction in this energy interval and the cross section increases strongly with the atomic number and e.g. a gas mixture based on Xe would be suitable to use. Another advantage of using a high atomic number gas, is that the electron range is shorter which improves the spatial resolution. It would still be a challenge to achieve a high detection efficiency in a gas volume that is not too thick. The efficiency could be improved

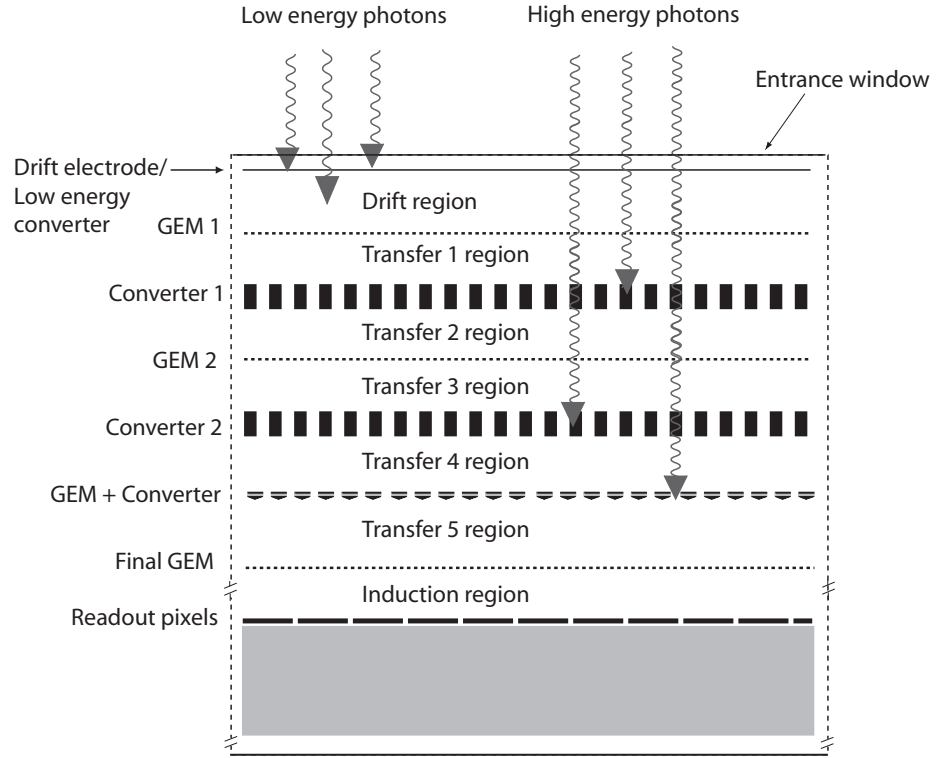


Figure 2.1: Schematic illustration of a possible detector geometry (not to scale). High energy photons interact in the converter plates and create primary electrons. Those electrons ionize the gas and the secondary electrons are drifted through the chamber down to the readout plate by the applied electric field. When passing a GEM the electrons are multiplied in order to compensate for losses in the following converter plates. Low energy photons will mainly interact at the top of the detector, either in the combined drift electrode/low-energy-converter plate or in the gas volume of the drift region (a thicker volume is needed). An idea is to increase the detector efficiency and reduce the detector thickness by combining the GEM and converter in one device, as is illustrated in the layer between the Transfer regions 4 and 5.

if the top electrode could be turned into an efficient converter for low energy x-rays, i.e. if it could be made of CsI for example [IV], in this case the depth of the detector volume required for diagnostic x-rays could be kept at a minimum.

Therapeutic energies

The vast majority of the impinging high energy photons pass through the top section of the detector without interacting, since the interaction probability here is very low. In the first metal converter plate a fraction of the photons interact by incoherent scattering and pair production, as will be the case in each consecutive converter plate. The emitted primary electrons or positrons will ionize the gas and note that the high energy electrons are not affected by the electric field in the detector.

During the radiation treatment there are scattered electrons and photons from the patient and the treatment couch that hit the detector. These will not contribute to the image information, but may disturb the image quality. The effect of those can be reduced by switching off the electric potential at the drift electrode and the first GEM when running in EPID mode. Thereby the scattered particles are attenuated not only in the chamber window, but also in the first converter plate. The entrance window of the chamber might also help reducing the number of scattered low energy electrons.

Collection of the secondary electrons

The signal in form of ionization will drift downwards through the electrical field generated by the increasing electrical potential at each layer. Starting with maximum negative potential applied at the drift electrode, to be reduced with approximately 1 kV/cm in the transfer regions and ending with the collector plate applied to ground potential. The transfer regions according to figure 2.1 operate in an ionization chamber mode, i.e. the electric field is strong enough to prevent recombination of the electrons and ions by drifting them in opposite directions along the field lines. The converter plates are perforated with holes to allow for the electrons to pass through. The area of the holes in the converter plate, relative to the area covered with material, is defined as the optical transparency, $T_{optical}$. Quite a large fraction of the electrons will be lost at each converter plate since they follow the electric field lines ending there. This loss is compensated for by increasing the number of electrons incident on the converter plate, by multiplying them in the amplification process in the previous GEM. The very last GEM, located immediately above the induction region as indicated in figure 2.1, can be operated at a higher gain, since here all the signals are unified and will be equally amplified. Finally the electrons are extracted to the pads of the readout plate at the bottom of the chamber.

2.1.1 The Gas Electron Multiplier

The Gas Electron Multiplier was invented by F. Sauli in 1996 [26]. The GEM is a thin structure of two metal electrodes with an insulating foil inserted in

between. The layer is perforated with holes, where the electron multiplication can occur when applying a potential difference.

The GEM typically consists of a $50\text{ }\mu\text{m}$ thin kapton foil coated with a $5\text{ }\mu\text{m}$ copper layer on both sides. It is chemically etched with double conical holes with a hexagonal pattern of holes according to figure 2.2. The diameter of the holes is $70\text{ }\mu\text{m} \pm 5\text{ }\mu\text{m}$ in the copper and $50\text{ }\mu\text{m} \pm 5\text{ }\mu\text{m}$ in the kapton, and the holes have a pitch of $140\text{ }\mu\text{m}$ resulting in a hole density of ~ 50 holes per mm^2 . There are other dimensions of the holes available, but this is the standard GEM geometry.

The GEM manufacturing technology has been developed at CERN in the printed circuits workshop by A. Gandi and R. De Oliveira [27]. The kapton covered with copper is coated with a photosensitive layer on both sides and exposed to UV light through a mask reproducing the desired holes' pattern. The metal is then chemically removed in the holes, and the foil is immersed in a solvent for kapton. Hence the manufacturing procedure creates conical holes from both sides.

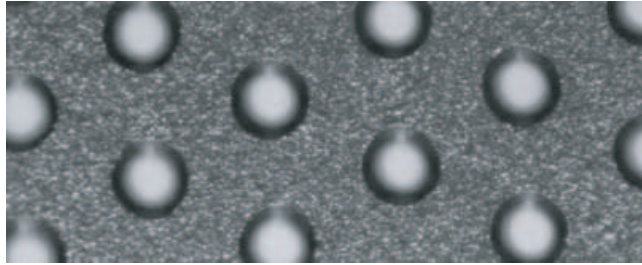


Figure 2.2: Photo of the GEM taken in a microscope. The holes are in a hexagonal pattern with a pitch of $140\text{ }\mu\text{m}$.

When applying an electric potential difference between the two electrodes, a strong electric field is focused within the holes of the GEM, see figure 2.3. If injecting an electron into a hole it will be accelerated by the strong electric field, and create an avalanche of secondary electrons. The total number of electrons produced can be controlled by the applied potential over the GEM electrodes, since the GEM is working in the region of proportional multiplication.

The ions created in the process move upwards, either to the GEM-top electrode or even further up in the structure. Some of the avalanche electrons will be attracted to the GEM bottom electrode, and the rest of them emerging from the hole and transferred down stream. Hence several GEMs can be put in cascade to further increase the signal. This is one of the features making the GEM a successful device in various detector applications over the world. Note that the multiplication in the holes is defined as the *real gain*, and the increasing number of electrons emerging from the GEM, as compared to impinging on it, is defined as the *effective gain*.

The GEM can be obtained from the workshop at CERN, and the active size of a standard GEM is either $5\text{ cm} \times 5\text{ cm}$, or $10\text{ cm} \times 10\text{ cm}$ [28]. Production of

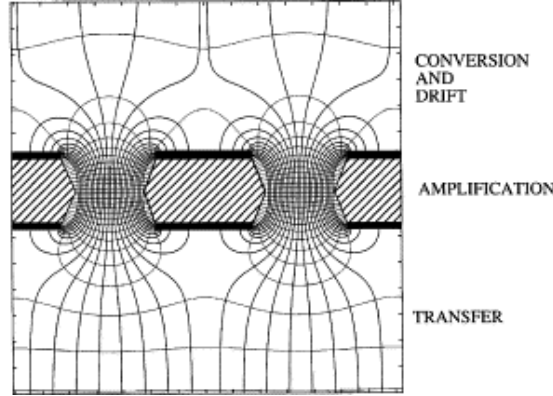


Figure 2.3: Electric field lines and equipotentials in the GEM holes on application of a voltage between the electrodes [30].

a size up to 2000 cm^2 is possible though [29] and e.g. the COMPASS tracking detectors are using large size ($31 \text{ cm} \times 31 \text{ cm}$) GEMs [31]. In this work standard GEMs ($10 \text{ cm} \times 10 \text{ cm}$), acquired from CERN, were used.

During some of the measurements the GEM was placed immediately on top of a Cu plate. In this way the anode position is in the center of the hole and therefore more electrons are collected, i.e. the signal measured is the real gain. This mode is named *Compteur A Trou*, CAT [32].

2.1.2 Gas mixture considerations

Many different variations of gas mixtures can be used with the GEM and one common composition is Ar-CO₂. Although not the best for obtaining the highest gain, it has the advantage to be non flammable, chemically stable, having a fast electron drift velocity and it is also intrinsically non-aging even under severe avalanche conditions [31]. However, the mean energy required to create an ion-electron pair by an incident electron, is 26 eV, 24 eV and 22 eV, for Ar, Kr and Xe respectively [33]. Therefore a somewhat larger number of secondary electrons (i.e. a larger signal) will be obtained per primary electron released from the converter plate in a Xe mixture.

Characteristic x-rays are emitted when the gas molecules de-excite or the ionized molecules attract a new electron to fill the gap from the emitted electron. Especially within the holes of the GEM, where the avalanche takes place, a lot of photons are emitted. Those photons are of various energies, depending on which shell the emitted electron originates from. Usually it is the K-shell electrons that are knocked out during the ionization. Those photons are emitted in all angles and if they are of sufficiently high energy they can create a photoelectron in the detector material elsewhere. They will blur the image if not absorbed by the converter plates in a short distance. Therefore a polyatomic gas, a so

called quencher, is mixed with the noble gas. CO_2 is a quenching molecule for example, and these molecules absorb the radiated photons and then dissipate the energy through dissociation or elastic collisions [33].

A high pressure system would produce more ion-electron pairs per track length of the primary electrons, but would be less convenient to work with.

2.1.3 Metal conversion layer for high energy photons

In the introduction it was mentioned that existing EPIDs are quantum limited. With the new detector, one can solve that problem by constructing a detector with many thin converter layers. Hence the overall attenuation is higher and a larger fraction of the generated electrons are extracted from each converter plate. Furthermore does the spatial resolution depend on the converter thickness, because the primary electrons are affected by multiple scattering and a wider spread of the electrons is noted when emerging from a thicker metal plate [34]. Hence it is advantageous to reduce the thickness of the converter plates. The thickness should be in the order of the range of the electrons created for a certain material and a certain energy.

The hole diameter and hole density will affect the quantum efficiency in such a way that more surface area available (many holes) will make it easier for electrons to emerge within the holes of the converter and thereby increase the quantum efficiency. Large holes and a high hole density will further increase the electron transmission through the converter. However, less material to interact with, will decrease the attenuation probability and therefore lower the quantum efficiency. This needs to be optimized, and one can conclude that thin converter plates are advantageous for both the electron transmission and reaching a high total quantum efficiency with a multilayer structure where many layers are feasible.

Note that the spatial resolution is limited by the hole pattern of the converters if the pitch is larger than the pixel size in the electronic readout system. It can never be higher than the pitch of the converter holes.

The choice of converter material can be regarded from several aspects; a high atomic number material will provide a high attenuation, i.e. a high quantum efficiency, on the other hand will the electrons created in the plate be subject to a higher probability of multiple scattering in that case, which would worsen the spatial resolution. A third aspect is that one should choose a material which is easy to handle and process.

In summarizing, the following parameters of the converter plates are important to optimize for the imaging application:

- Thickness
- Number of layers

- Hole diameter
- Hole density
- Material properties

2.1.4 Electronic readout system

A pixelized readout system is needed to extract the electrons created in the detector. The requirements on such an electronic readout system is quite demanding. About 200.000 pixels covering an area of $40\text{ cm} \times 50\text{ cm}$, with an $1\text{ mm} \times 1\text{ mm}$ spatial resolution, should be read out in parallel at a speed of 200 fps if possible. The radiation environment at a treatment facility is harsh, the photon fluence rate is large, in the order of $10^{10}\text{ photons mm}^{-2}\text{s}^{-1}$ during the pulses. Hence it is likely that electronics placed in such a beam would be damaged.

With those requirements in mind, the research group in collaboration with R. Kihlberg [35] came up with the idea of a new electronic readout system solving the problems pointed out above and a possibility to route out the signal from the large number of pixels. All collector pads are placed on the edge of an ordinary printed circuit board¹, and the signal can then be routed through a trace from each pad to the end of the FECs where the electronics is situated well outside the beam.

A prototype of the electronic readout was manufactured by Gamma Medica-IDEAS [36] and delivered with a complete control system including software. The FEC is implemented as an array of a 4-layered printed circuit board, see figure 1 in [V]. A trace goes along the FEC from each single pad to the Application Specific Integrated Circuit, ASIC, attached at the side of the array. In this way each pad can be read out in parallel. The FECs are stacked close to each other, forming a 2D area of 50×100 pixels, see figure 2 in [V]. The prototype has got a pixel size of $1.27\text{ mm} \times 1.27\text{ mm}$, which corresponds to $0.98\text{ mm} \times 0.98\text{ mm}$ at the isocenter with a Source to Detector Distance (SDD) of 130 cm (which corresponds to a typical clinical imaging distance [16]).

The system can be further described by the components shown in figure 2.4. The double sample and hold (S/H) functions and the parallel traces to all pads guarantees the fast speed of the imaging detector. During the integration time the electrons are collected at the pads and extracted to the individual charge integrating amplifiers located at the ASIC, figure 2.5. The integration amplifier converts the charge to a proportional voltage, which is sampled in one of the S/H channels. Data is shifted out from one unit while the other unit is active sampling the signal. In this way the readout deadtime is reduced to the reset time of the amplifier. The minimum reset time is $1\text{ }\mu\text{s}$ according to the supplier, while $10\text{ }\mu\text{s}$ was used during the tests. The readout time for all channels is 4.3 ms, i.e. the time it takes to shift all data out from the S/H units, convert it to

¹We denote this a Front End Card, FEC.

digital format in the Analog to Digital Converter (ADC) and transfer it to the computer. The temporal resolution is therefore less than 5 ms and a frame rate exceeding 200 Hz is achievable. It is believed that the ASIC and the general readout strategy could be modified to handle any frame rate that would be of interest in radiation therapy imaging.

Further specification and information about the electronic readout system can be found in [V] and in the patent that was issued in 2005 [37].

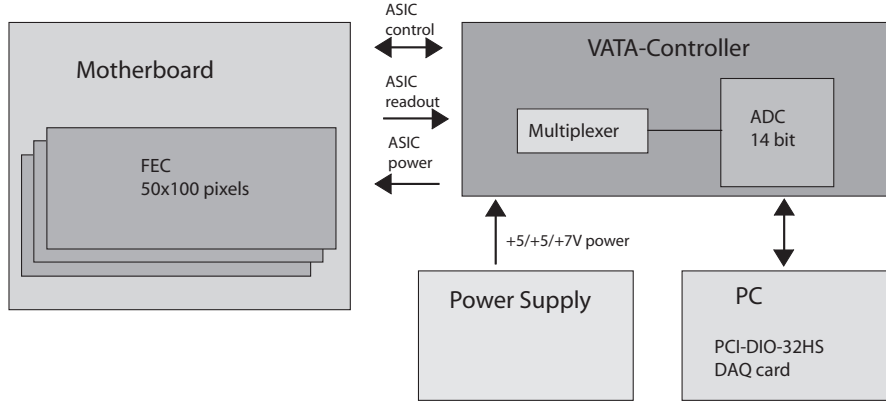


Figure 2.4: Schematics of the electronic readout system.

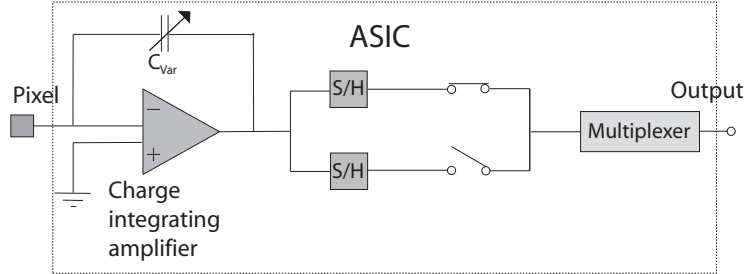


Figure 2.5: The structure of the ASIC.

2.2 Estimation of achievable detector efficiency

The PENELOPE Monte Carlo code [38] was used to estimate the achievable quantum efficiency of the detector. In the estimation it was assumed that there are no signal loss during the electron transport in the gas, and that the multiplication in the GEM will fully compensate the absorption losses of electrons in the converter plates. The converter geometry was set to an infinitely wide slab of either Cu or W without holes, and the thickness was varied from 10 μm to 5 mm. For each layer thickness more than 10^7 photon events were generated. The incident photon energy was either monochromatic at 1.7 MeV or a

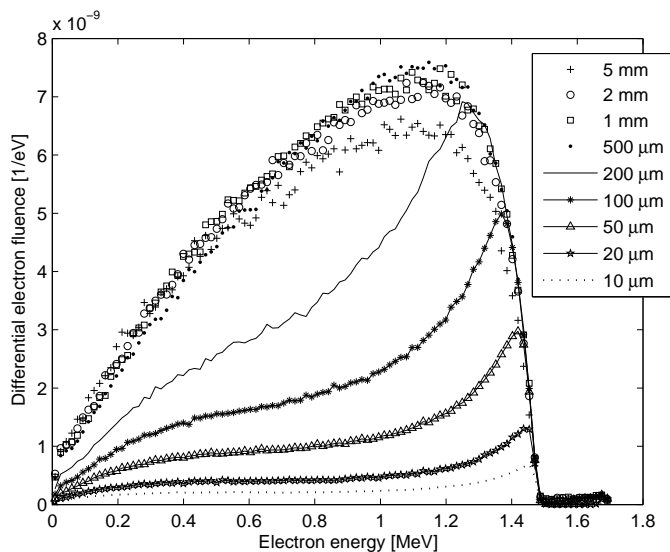


Figure 2.6: The energy spectrum of the electrons emerging from a Cu plate of various thickness. The electrons were created by 1.7 MeV photons interactions in the plate. The spectra were calculated with the Monte Carlo code PENELOPE [38]. A spectrum skewed as in figure 2.7 would be more realistic for a true 6 MV beam.

18 MV photon spectrum. The attenuation of the mono energetic beam corresponds approximately to the mean energy of a low energy treatment beam of 6 MV (calculated with the EGS4 Monte Carlo code, BEAM) [39], and the 18 MV spectrum corresponds to a Varian accelerator and was obtained from [40]. Incoherent scattering, the photoelectric effect and the pair production processes were all included. The particles (all generations) were traced down to a final energy of 10 keV or less for all particles. At this energy level they were considered to be locally absorbed in the metal.

The energy spectrum of the electrons emerging from the metal slab (at the bottom side) is presented in figures 2.6 to 2.8. The spectra include both primary electrons and electrons generated in secondary processes. The primary electrons however constitute more than 98% in the mono energetic beam and 94-97% for the 18 MV spectrum.

The quantum efficiency, QE, is here defined as the fraction of incident quanta that will interact in a converter plate *and* generate primary electrons that will escape from the plate and contribute to the signal. Knowing the cross section for interaction of the photons in the converter plate and the probability for the primary electrons to emerge from the converter plate, the QE can be estimated as indicated in figures 2.9 and 2.10.

The compton process is the dominating photon interaction for the mono energetic photons simulated, and therefore it is reasonable to assume that a max-

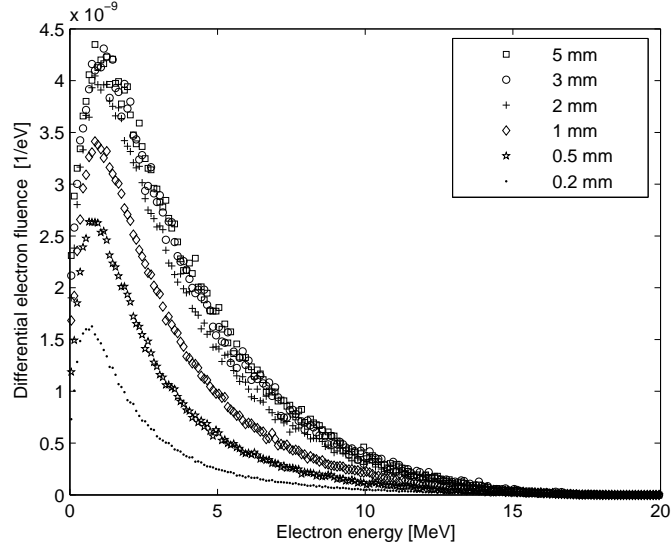


Figure 2.7: The energy spectrum of the electrons emerging from a Cu plate of various thickness. The electrons were created by an incident 18 MV spectrum and secondary processes in the plate. The spectra were calculated with the Monte Carlo code PENELOPE [38].

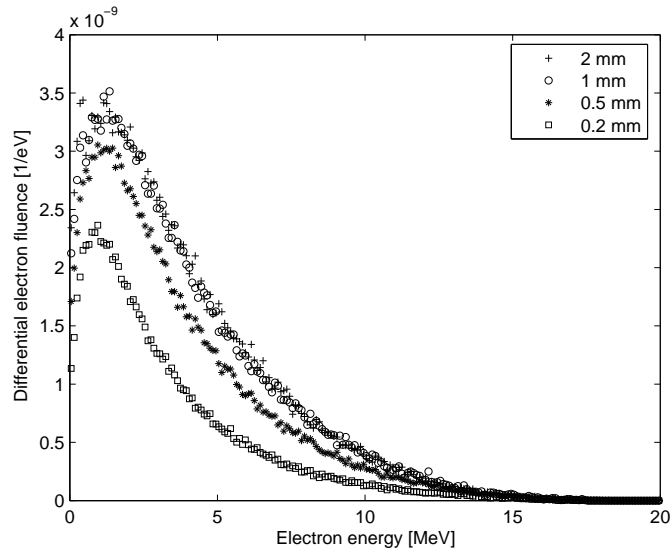


Figure 2.8: The energy spectrum of the electrons emerging from a W plate of various thickness. The electrons were created by an incident 18 MV spectrum and secondary processes in the plate. The spectra were calculated with the Monte Carlo code PENELOPE [38].

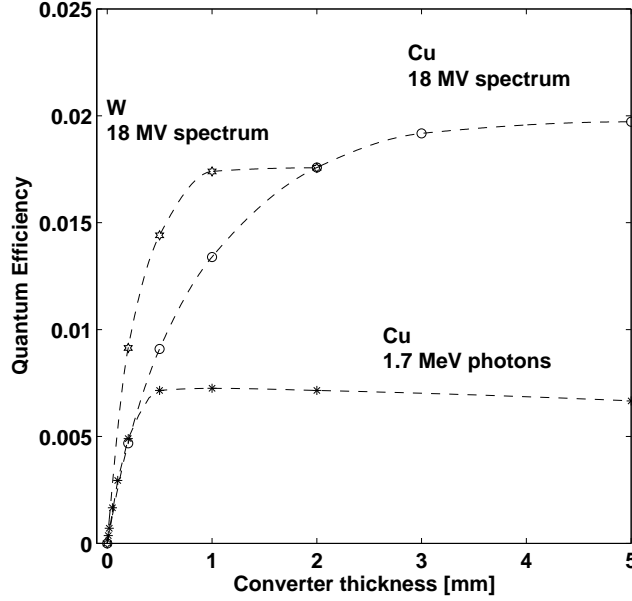


Figure 2.9: The quantum efficiency for 1.7 MeV photons impinging on uniform Cu plates of increasing thickness from 10 μm to 5 mm. The quantum efficiency for an incident 18 MV spectrum on uniform Cu and W plates are also included.

imum QE is achieved when the thickness of the converter plate is below the practical range of the compton electron, i.e. the thickness when electrons do not have enough energy to emerge. With an incident photon energy of 1.7 MeV, the maximum energy of the compton electron is 1.48 MeV (compton edge), and is achieved when the photon is backscattered in 180° . The practical range (half the CSDA range) is 560 μm for 1.48 MeV electrons in Cu [41, 42].

As mentioned previously, one should also consider the correlation of spatial resolution with the thickness of the converter plates as illustrated in figures 2.11 and 2.12, where the angular distribution of the emitted electrons (primary and all later generations) from a Cu and a W plate of several thicknesses can be seen. It is clear that the electrons emerging from a thick converter plate are more divergent compared to the electrons escaping from a thinner plate [43]. Further is the angular distribution slightly shifted toward larger angles for electrons emitted from a W plate of 0.5 mm thickness if compared to a Cu plate of the same dimension for example. The reason is as mentioned before, that W has a higher atomic number than Cu and therefore the electrons are subject to a stronger multiple scattering.

If assuming perforated converter plates with a transparency $T_{\text{optical}} = 23\%$, as defined in section 2.1, the estimated QE of any converter plate (i) in the multilayer structure (assuming unit electron amplification in each layer) may be approximated by

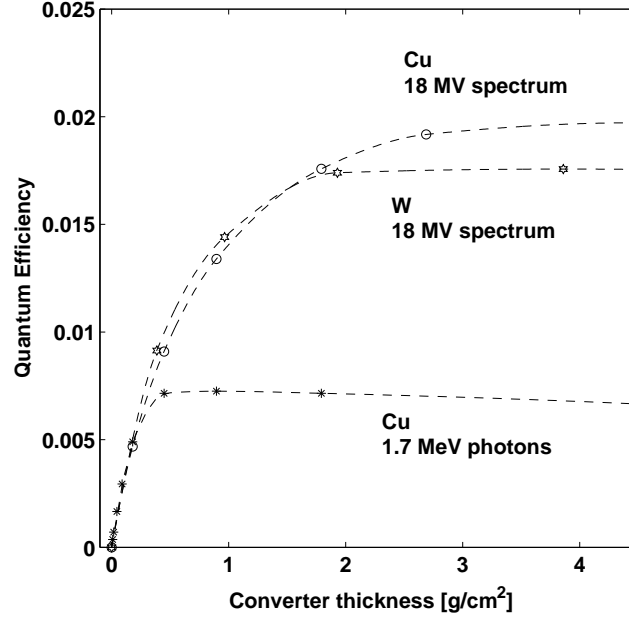


Figure 2.10: The same quantum efficiency as presented in figure 2.9, however here the thickness is specified in the unit g cm^{-2} . By applying this unit one can see the variation in the QE as a function of the atomic number alone for the different materials included.

$$QE(i)_x = QE(1)_x \cdot (1 - T_{\text{optical}}) \cdot [1 - (1 - e^{-\mu x}) \cdot (1 - T_{\text{optical}})]^{(i-1)} \quad (2.1)$$

where $QE(1)_x$ is found for each plate thickness (x) in the data shown in figure 2.9, and μ is the linear attenuation coefficient. The quantum efficiency of a detector with N converter layers then becomes

$$QE(N)_x = \sum_{i=1}^N QE(i)_x \quad (2.2)$$

The simulation data provides information about the total probability for the attenuation considering all energies in the spectrum, and using the separate attenuation value for each converter thickness, the QE can be roughly estimated for many layers. In the case of the mono energetic beam, tabulated values of the linear attenuation coefficient were used [44]. The QE for up to 200 layers is presented in figure 2.13. The results show that it is possible to reach a higher QE using thin converter plates at the cost of a large number of layers.

The limit of the maximum QE for each thickness is defined by the fraction of emitted primary electrons per attenuated incident photons. This ratio is higher

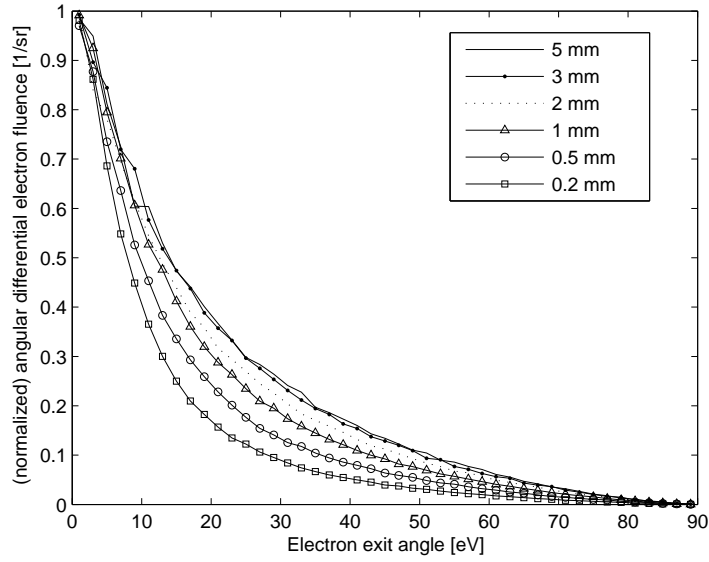


Figure 2.11: The angular distribution of all electrons emitted from a Cu plate of indicated thickness. The data is from the Monte Carlo simulation of the incident 18 MV spectrum.

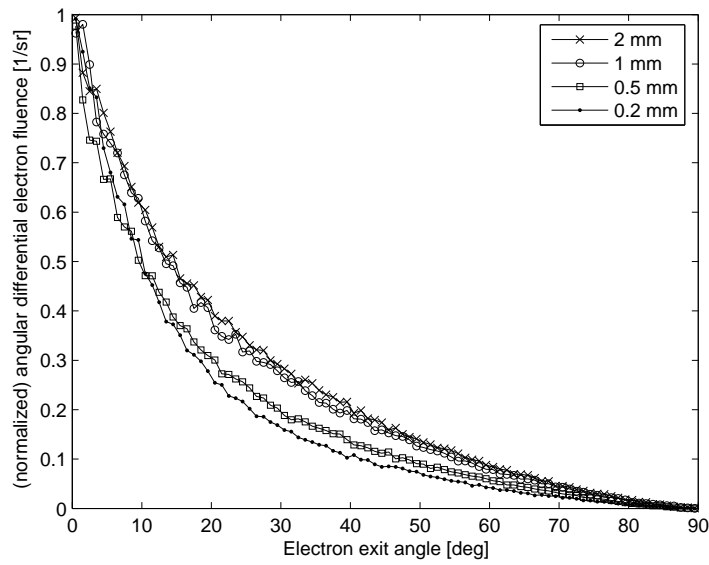


Figure 2.12: The angular distribution of all electrons emitted from a W plate of indicated thickness. The data is from the Monte Carlo simulation of the incident 18 MV spectrum.

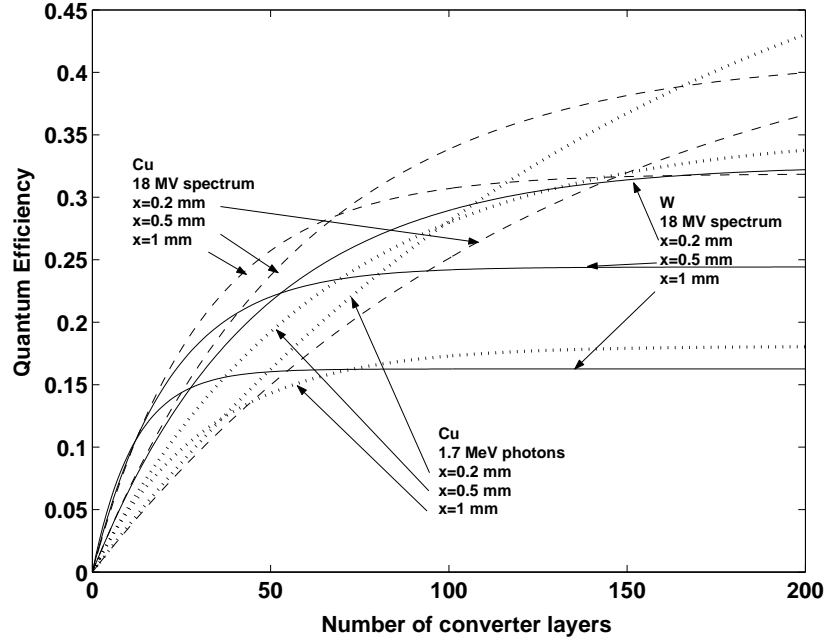


Figure 2.13: The estimated quantum efficiency of the detector based on equation 2.2 for 1.7 MeV photons (dotted line) and an 18 MV spectrum incident on a Cu plate (dashed line) and a W plate (solid line). The QE increases with the number of converter plates until most of the photons are attenuated and the maximum QE is reached for that specific converter thickness.

for Cu than for W, hence if assuming a very large number of converter plates, a higher QE will be reached with the Cu plates.

From a practical point of view, it may be feasible to include 10-20 layers for a portal imaging application. The estimation indicates that in case of Cu, converter plates in the order of 0.5 mm will be the most advantageous to use for 1.7 MeV photons and 2 mm thick converter plates for the 18 MV spectrum, see figure 2.14. For 20 layers a QE of 9.5% and 16% can be achieved for 1.7 MeV photons and a 18 MV spectrum respectively. The 18 MV spectrum incident on a 0.5 mm W converter plate provides a QE of about 15%, almost 10 times the value of AMFPIs.

The results show that almost the same QE can be achieved for 1 mm Cu plates as for 0.5 mm W plates, in the range of 10-20 layers. It is advantageous to use thinner plates since it reduces the total detector thickness for example. However, if comparing the angular distribution of the emitted electrons from a 0.5 mm W plate to a 1 mm thick Cu plate, the electrons from the W plate are somewhat more divergent than for the Cu plate as indicated in figure 2.15.

The thickness of the active detection volume must not exceed 2-4 cm, or the parallax error will limit the spatial resolution towards the edges of the detector.

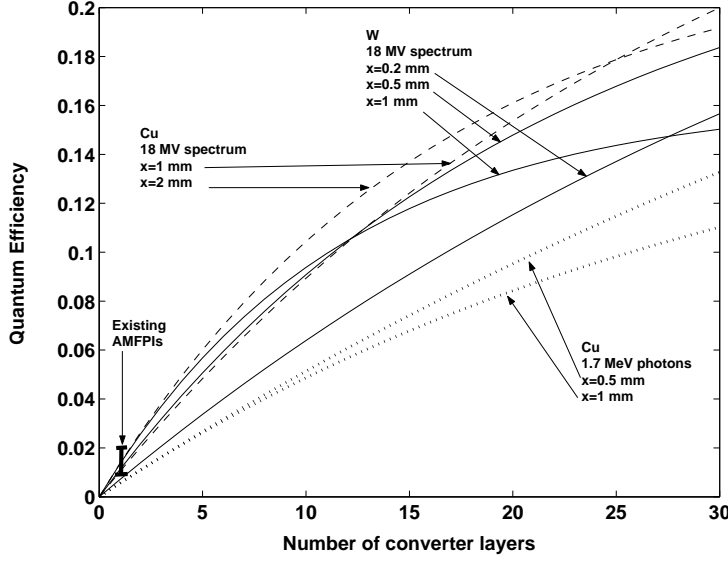


Figure 2.14: This is an enlargement of figure 2.13 (with some thicknesses exchanged for others). It shows that for a 20 layer structure, the highest QE is achieved for converter plates in the order of 0.5 mm for 1.7 MeV photons incident on Cu, and 2 mm for a Cu plate and 0.5 mm for a W plate when irradiating with an 18 MV spectrum. For comparison, the range of the quantum efficiency of existing AMFPI systems has been included (maximum $\sim 2\%$).

To reduce the thickness of the detector one could think of combining the GEM and the converter plate to one device. Another way of mitigating the effect of parallax would be to segment the detector in such a way that the normal to each segment points back to the source using a cylindrical or spherical detector.

In these estimations of the QE for a multilayer structure, secondary photons were not accounted for. Those photons may give rise to a signal when interacting in converter plates further downstream in the detector. If the primary photon was already registered this will lead to a double (or multiple) registration of one primary photon. In the cases when the primary photon was not registered before, these secondary processes will increase the QE. However, the secondary processes will also decrease the spatial resolution depending on the scatter angle of the photons. Again a thin detector is desirable.

The photons detected below a converter plate is dominated by the transmitted incident photons as seen in figure 2.16, and therefore the detected photon energy distribution is very similar to the incident spectrum. However, one can note that for a 5 mm and a 2 mm Cu thickness, there is a peak at ~ 500 keV. This is due to the positron - electron annihilation within the metal, and these photons will be emitted uniformly and appear as a scattered background in the detector.

Full Monte Carlo simulations including the whole detector design should be per-

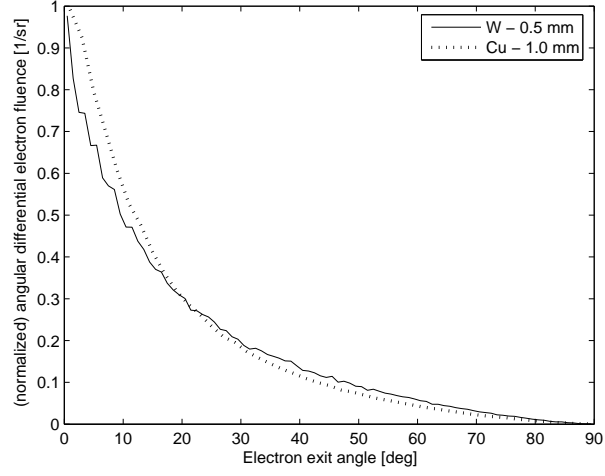


Figure 2.15: Comparison of the angular distribution of emitted electrons from a W plate of 0.5 mm and from a Cu plate of 1 mm thickness. The data is from the Monte Carlo simulation of the incident 18 MV spectrum. The electrons from the W plate diverge slightly more than the electrons from the Cu plate.

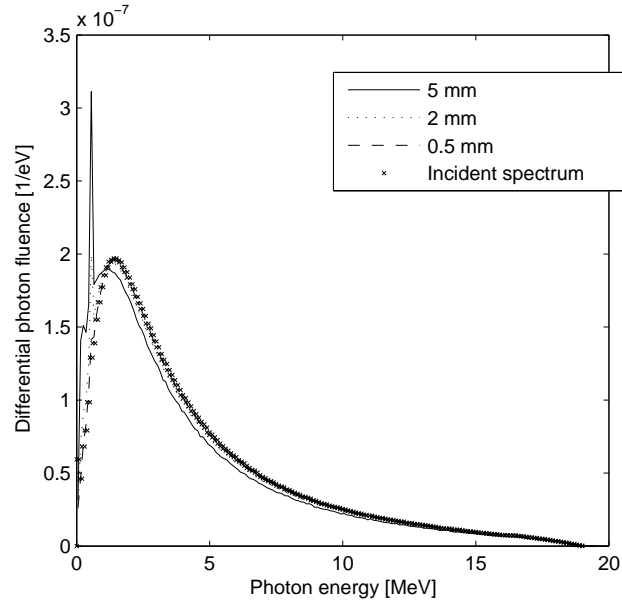


Figure 2.16: The energy spectrum of the photons (transmitted, secondary and scattered) detected under a Cu plate of various thickness. The spectrum is dominated by the transmitted primary photons from the incident 18 MV spectrum. The spectra were calculated with the Monte Carlo code PENELOPE [38].

formed in order to optimize the QE and spatial resolution of the detector. A possible signal contribution from the electrons emitted from the inner surface of the holes could in this case be accounted for, and it may for small holes give a positive contribution. The optimization parameters for the converter plates listed in section 2.1.3 could be used as a starting point. The electric field strengths and charge transport in the transfer fields must be considered, and also the GEM multiplication. The full energy spectrum of the accelerator of interest should be considered when optimizing the detector components and functions.

Chapter 3

Experimental realization

Two prototypes of the new detector were built. The first one for general GEM measurements, and the second for imaging. The basic functions of the detector components were tested experimentally in the x-ray laboratory of the Particle and Astroparticle Physics group at KTH and at the Karolinska University Hospital, Stockholm.

3.1 Materials

3.1.1 Diagnostic x-ray beam (~ 50 kV)

High rate measurements were performed not only with high energy photons, but also with low energy x-rays. Two x-ray tubes, Kevex (max 50 kV and 0.1-1 mA) and Philips PW 1830/40 (10-60 kV and 10-60 mA) were used. The photon fluence rate for the Philips x-ray tube was measured independently with a semiconductor detector (XR-100T-CZT, Amptek) that was connected to a multi channel analyzer (Pocket MCA8000, Amptek), and placed behind a collimating slit at 3.5° and approximately 1 m from the x-ray tube. The horizontal slit was 10 μm wide and the vertical slit size was varied between 10-300 μm , depending on the photon beam intensity. The measured photon fluence rate is presented in figure 3.1. Some values were compared to an energy spectrum for a wolfram target with a 1 mm Be window and 0.5 mm Al filter, and the photon fluence rate was found to be in the correct order of magnitude [45]. Since no filter was used in the measurement, a higher fluence rate is expected compared to the reference. The fluence rate of the Kevex x-ray tube was not calibrated with an independent detector as for the Philips tube. However, having the same target it was assumed that the photon fluence rate was scaling linearly with the spectral data reference [45].

For comparison, the incident photon fluence rate was estimated from the ion-

ization chamber currents measured with the detector at two occasions. The Philips and the Kevex tubes were set to 30 kV. For the Philips tube, the estimated fluence rate was $2.9 \cdot 10^7$ photons $\text{mm}^{-2}\text{s}^{-1}$ at the location of measurement (SDD=38 cm), and the independently measured fluence rate $3.4 \cdot 10^8$ photons $\text{mm}^{-2}\text{s}^{-1}$ at the same distance, while the referenced fluence rate was $8.9 \cdot 10^7$ photons $\text{mm}^{-2}\text{s}^{-1}$. In the case of the Kevex tube, the estimated fluence rate was found to be $2.3 \cdot 10^7$ photons $\text{mm}^{-2}\text{s}^{-1}$, while it was $1 \cdot 10^8$ photons $\text{mm}^{-2}\text{s}^{-1}$ according to the reference. Hence the values are in the same order of magnitude even if the estimated photon fluence rate was somewhat low.

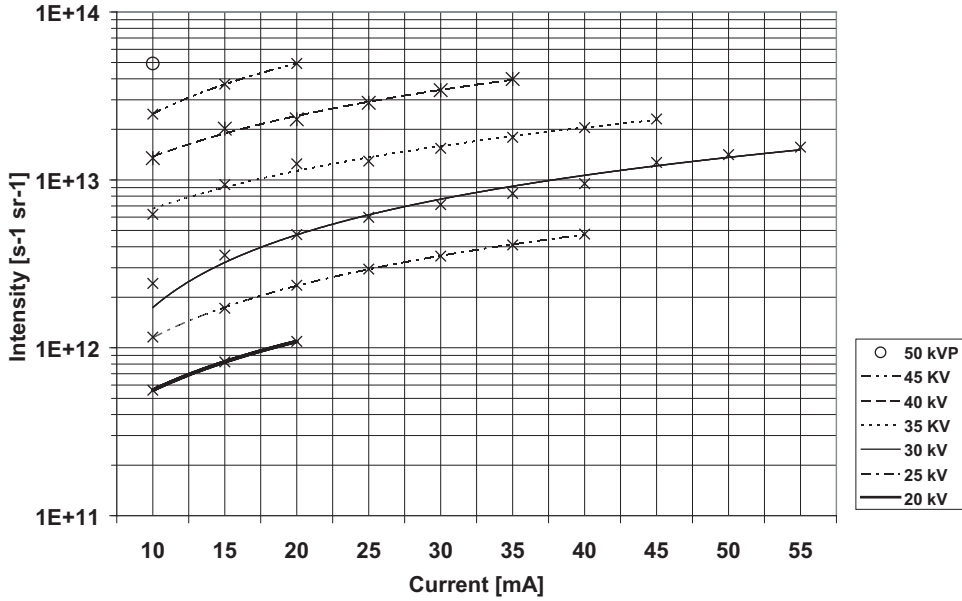


Figure 3.1: The photon fluence rate at the Philips x-ray tube measured with an independent detector.

3.1.2 Therapeutic Racetrack microtron beam (~ 50 MV)

The high energy measurements were made at the Racetrack microtron¹, an accelerator for radiation therapy used at the Karolinska University Hospital in Stockholm. The accelerator provides uniform bremsstrahlung beams with up to 50 MeV peak photon energy with a scanning narrow photon pencil beam. No beam flattening filter is used in this device, therefore the mean energy is higher than for any other conventional accelerator. Tests were performed at a dose rate to water of $\dot{D}=2$ Gy min^{-1} at isocenter, with an assumed photon mean energy of 18 MeV [46]. The photon fluence rate is obtained using the relation $\dot{D} = \phi \cdot h\nu \cdot \frac{\mu_{en}}{\rho}$ assuming charged particle equilibrium. With the mean

¹The Racetrack treatment accelerator at the Karolinska University Hospital in Stockholm is generally operated at 50 MV acceleration potential.

energy $\overline{h\nu}=18$ MeV and the mass energy absorption coefficient $\frac{\mu_{en}}{\rho} = 0.0141$ cm^2g^{-1} [44] the average photon fluence rate is $\dot{\phi} \approx 8 \cdot 10^6$ photons $\text{mm}^{-2}\text{s}^{-1}$. The Racetrack is pulsed with 3-5 μs long pulses at a frequency of 200 Hz. The pulse corresponds to a peak photon fluence rate in the order of $\dot{\phi} \approx 1 \cdot 10^{10}$ photons $\text{mm}^{-2}\text{s}^{-1}$. This beam was used in publications [III, IV].

3.1.3 Test chambers

An existing aluminium chamber (chamber 1) was adapted for the GEM measurements and is shown in figure 3.2 A). A simple Cu plate was used as collector plate and the drift electrode was made of a Cu mesh in most cases. The photo in figure 3.2 B) however shows the high energy setup when a solid Cu plate was used as a combined drift electrode and converter. Nylon screws were holding the parts together, with a thick PMMA (Polymethyl Methacrylate) plate as a base, see figure 3.2 B). Frames for the GEM foils and also the distances that separate the layers were made of PMMA in this setup. This chamber was used in publications [I-IV].

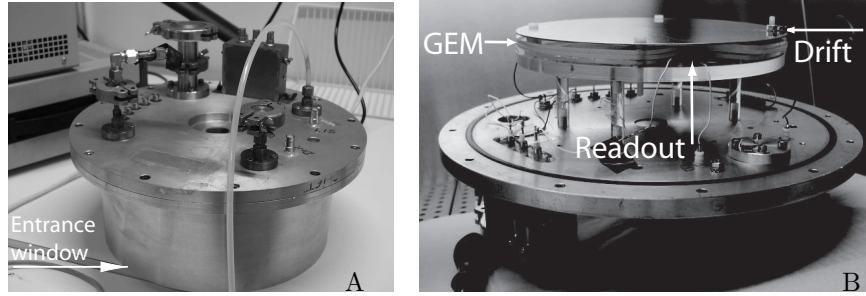


Figure 3.2: A) Photo of test chamber 1. B) A single GEM installed with a 1.5 mm Cu plate mounted as drift electrode and a plain Cu plate as collector.

A stainless steel chamber (chamber 2) with a 12 mm thick top and bottom lid was designed and built to hold the dedicated electronic readout developed for the application, see figure 3.3 A). SHV feed through contacts and gas inlet/outlet were added to the bottom lid. The entrance window is made of 0.3 mm Al foil and is located at the top lid and has a size of 137 mm x 75 mm. New layer distances and frames for the GEM and the drift electrode were constructed in the more radiation resistant material Rexolite, see figure 3.3 B). A Cu mesh was used as a drift electrode in this chamber as well. This chamber was used in publications [IV, V].

3.1.4 High voltage supplies

A number of high voltage (HV) supplies were used during the first part of the study, e.g. Tennelec TC950, Oltronix A2,5K-10HR and Fluke (72419) 415B High

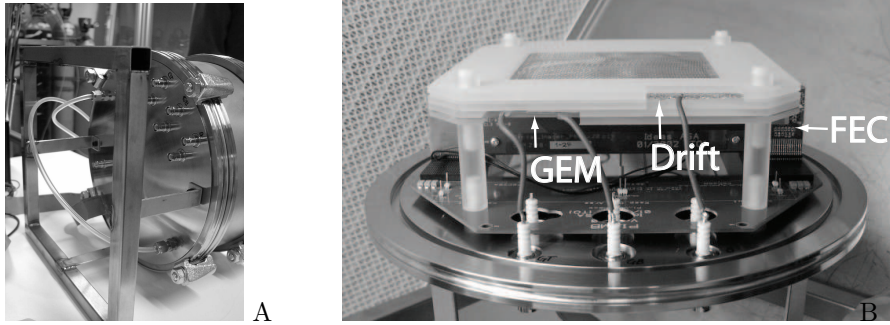


Figure 3.3: A) Photo of test chamber 2. B) A single GEM setup installed in the chamber with Cu mesh as drift electrode, and the 50 FECs are installed as readout.

Voltage Power Supply. They were either individually powering the electrodes in the chamber, or the voltage was supplied via resistor chains in the case when being limited by the number of available HV feed through contacts in chamber 1.

Floating HV-supplies were constructed for the second part of the study, when the 50 FEC pixelized readout was installed. The modules had a continuous voltage range of up to 0.5, 1 and 2 kV for two modules respectively, i.e. there are six HV modules in total. They were very convenient to use in the laboratory environment where the potentials are to be varied repeatedly.

3.1.5 Experimental procedures

Standard GEMs obtained from the CERN workshop [27] were used during the tests, see section 2.1.1. The GEM was stretched by hand and attached to the frame with double sided tape. This is a very primitive way of framing the GEM and visible wave pattern are seen on the foil, e.g. see figure 3.11.

All parts, except the GEM foils, had to undergo a thorough cleaning procedure before being mounted in the chamber. Cleanroom gloves, dishwashing liquid, de-ionized and distilled water, alcohol and an ultrasonic bath were tools in the lengthy process. After being blown dry with nitrogen or Ar-CO₂, the parts were installed in the chamber at the clean bench Telstar AH-100.

Protective resistors (in M Ω range) were connected in series with the GEM electrodes in most measurements. Large currents (μ A) at the GEM electrodes creates a voltage potential over the resistors, i.e. resulting in a voltage drop over the GEM during irradiation. The voltage was measured with Fluke 79 III multimeters and corrected when relevant.

The normal procedure is to flush through the gas for up to one day if the chamber has been opened previously, or heavily for a couple of hours if not operated for

some time. The normal operating gas flow is set to approximately 0.5 ml per second for the 5300 cm³ large chamber volume (chamber 2), and was controlled with a bubbler. The gas mixtures used during the study were Ar-CO₂(80-20) and Kr-CO₂(90-10) at atmospheric pressure.

3.2 Experimental results

Several of the experimental results are already published in the included publications [I-V]. A number of other experiments were also conducted and described below.

3.2.1 Data acquisition system

As a first step 6 FECs were mounted in chamber 2 in a single GEM mode. The drift region was 6 mm and the induction region 3 mm thick. The gas mixture used here was Ar-CO₂(80-20). Basic functions of the readout electronics were tested, e.g. the range of the ASIC linearity was defined. A crude way of testing the position resolution was made by imaging a 0.5 mm wide slit. The result was presented in [V] and shows that the spatial resolution with a 6 mm thick drift region will be limited by the photoelectron range, and a less thick gas layer in the drift region should be implemented. However, a much thinner slit should be used in such an experiment and further measurements must be made in order to define the spatial resolution.

When satisfied with the basic tests, 50 FECs were installed with the single GEM setup. The drift region was reduced to a thickness of 3 mm though. Further verification measurements were made, but also imaging with the Philips x-ray tube.

Verification of the charge integration time

Tests were made to verify the charge integration time for the whole system. X-ray images were acquired of a copper disc (70 mm in diameter) rotating with a synchronous motor at a speed of 25 rps. The integration time of the readout system was set to 10 ms and 30 ms, which corresponds to 1/4 and 3/4 of a rotation respectively. Two holes of different diameters (8 mm and 10 mm) were drilled in the copper, and figure 3.4 shows how the disc was slightly tilted in order to avoid the motor in the beam. The results are displayed in figure 3.5, and they show that the integration times tested agree with the specification.

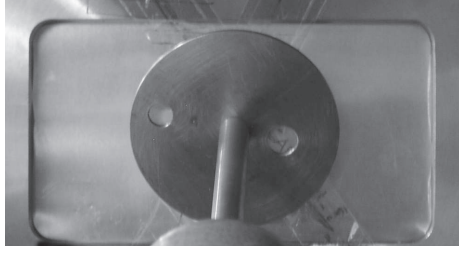
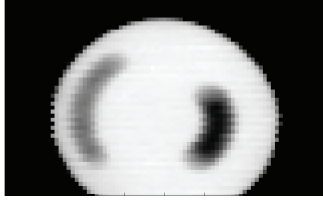
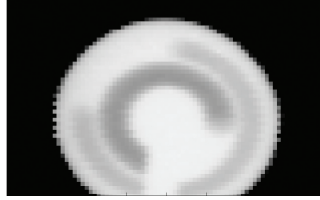


Figure 3.4: Photo of the copper disc attached to the axis of a synchronous motor used for verification of the integration time.



A.



B.

Figure 3.5: Verification of the charge integration time. A) An image of the Cu disc when the integration time was set to 10 ms. B) The integration time was 30 ms. The axis of the motor is seen at the bottom of the image.

Verification of the readout speed / Real time dynamic imaging

As described in [IV-V], alpha particles were imaged in real time with the 6 FEC setup. The integration time was set to 1 ms and the activity of the ^{241}Am source (~ 5.5 MeV) was in the order of 1 event per ms. Only one sample and hold unit per ASIC was utilized at the test, i.e. the frames were read out sequentially, and the imaging rate was 188 fps. The alpha particles tracks were displayed on a computer screen by the readout software, and the screen output was recorded in real time with a digital camera. However, the present software and the computer capacity, were limiting the actual viewing rate.

To further demonstrate the speed capacity of the readout system, a Newton pendulum was imaged with the 50 FEC setup. The five pendulum balls were made of stainless steel and had a size of 25.4 mm in diameter. The images were acquired with a 40 kV x-ray spectrum and a charge integration time of 10 ms, which corresponds to a frame rate of 70 fps. The acquired single frames were serially added to form a movie, and one of the frames is shown in figure 3.6.

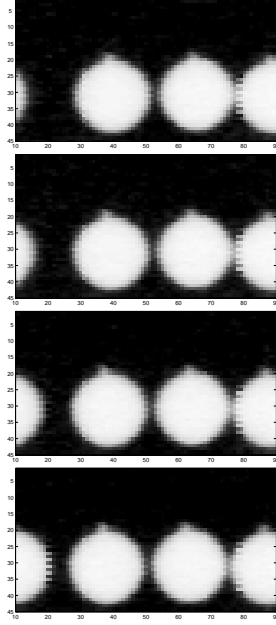


Figure 3.6: A series of consecutive images of the Newton pendulum when imaged at a frame rate of 70 fps. One of the balls is seen swinging in from the left.

3.2.2 GEM measurements

The GEM was a rather new device at the time when this project started and therefore general functions of the GEM were confirmed [I-VI]. Up to 3 GEMs were installed in chamber 1 and current measurements were performed at diagnostic energies (10-60 keV) with both x-ray tubes. A single GEM setup, see figure 3.2 B), was tested at treatment energies of a 50 MV spectrum. The current was measured with a Keithly 602 Electrometer. Further were pulse mode measurements made with the isotope $^{133}_{56}\text{Ba}$ decaying to $^{133}_{55}\text{Cs}$, emitting γ -rays of 81 keV and 356 keV, and characteristic x-rays of 31 keV. The signal was monitored on an oscilloscope HP 54645D via a fast linear amplifier, Ortec 572, and a charge sensitive pre-amplifier, Ortec 142PC, connected to the readout plate.

Useful information about the GEM characteristics was found when checking the the status of each foil, for example is the leakage current of a fully working GEM in the order of pA, and the capacitance approximately 5 nF (measured with Bridgometer TTi LCR400). Further was it noticed that the GEM could be conditioned (named 'training effect' in paper [I]) by operating it for some time in low energy x-rays. After a few discharges, a higher maximum achievable gain (i.e. the highest achieved gain before the first breakdown appear) could be obtained. The reason is probably that small irregularities or dust particles are burnt away by the discharges.

To display the level of multiplication versus the applied potential difference over

the GEM electrodes, a typical gain curve is presented in figure 3 in [I]. The gain is linear in a logarithmic scale. The gain curves of the CAT (GEM placed on top of the readout plate) and the GEM exemplifies the difference between the *real gain*, and the *effective gain*, as explained in section 2.1.1. This data was obtained for the gas mixture Ar-CO₂(80-20), and 30 kV and 10 mA applied on the x-ray tube, which corresponds to a photon fluence rate higher than 10^6 photons mm⁻¹s⁻¹. Even larger amplifications were achievable with a third GEM installed. In that case an overall gain exceeding 10^5 was obtained when the potential drop over the top GEM was $\Delta G1=400$ V, the middle GEM $\Delta G2=452$ V and the bottom GEM (placed in CAT mode) $\Delta CAT=347$ V, according to [I].

For this application, imaging in radiation therapy, the GEM has to stand very high photon fluence rates and manage large currents while still performing a linear and stable electron multiplication.

As displayed in figure 3.7, the GEM multiplication was operating linearly in a logarithmic scale also in the treatment beam. A single GEM was installed with a 0.2 mm thick Cu plate mounted as a combined drift electrode/ converter plate. The area irradiated was varied as indicated in the figure, and the accelerator was operated at 50 MV. The photon fluence rate was 10^{10} photons mm⁻²s⁻¹ during the pulses. Included in the plot is the gain curve for the single GEM tested with 30 keV x-rays from above. Both test setups were operating in Ar-CO₂(80-20). The results show that the amplification is similar independently if operated in a high energy treatment beam, or with low energy x-rays.

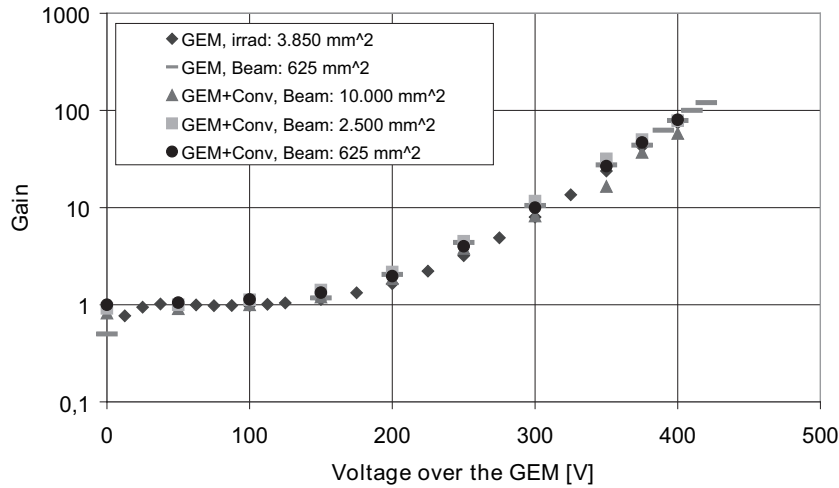


Figure 3.7: Gain curve of a single GEM tested in the Racetrack. The gain curve for 30 keV x-rays is included for comparison, and it can be seen that the amplification is the same, whether for high energy or low energy photons. As indicated, different areas were irradiated in the treatment beam and the gain curves are similar.

The maximum achievable gain for a single GEM was only $\sim 10^2$ during the tests at the Racetrack accelerator. This is rather low compared to the gains of 10^3 - 10^4 , that was obtained with the radiation from the x-ray tubes, see for example [III].

As mentioned in paper [I-III], an 'area effect' and a 'rate effect' has been observed during the studies. Those effects appears as a drop of the maximum achievable gain with the irradiated area and also with an increasing photon fluence rate. Especially when measuring single pulses from a radioactive source (i.e. in a much lower fluence rate), the GEM could be operated at a higher potential, see figure 5 in [I]. Since very high photon fluence rates are incident during short pulses in the treatment beam, the rate effect might be the explanation to why a lower maximum achievable gain is reached as compared to in the x-ray beam. However, further studies must be made in order to investigate this effect.

As in all micropattern gaseous detectors, discharges might occur in the GEM. The GEM is known for its reliability in the electron amplifying structure against discharges, however after certain amount of discharges, the GEM will inevitably fail. In a study with a triple GEM layer operating in a Ar-CO₂-CF₄(45-15-40), it was found that the GEM foils could stand 718, 819 and 931 discharges respectively [47]. However, to assure a long life time of the detector it is better to find a range of safe operation. With heavily ionizing particles present, the risk of inducing a discharge increases. At the high photon energies used in a treatment beam, photo nuclear reactions are possible (even though at a low probability) and the created neutrons might in turn create heavily ionizing particles. Therefore a study of discharges was made with alpha particles and x-rays. The conclusion was that the GEM should be operated at a gain below 10^2 to be in the safe region, not risking discharges. Tests performed at a treatment accelerator confirmed the results, see above and [III]. During the same test series as presented in figure 3.7, a discharge was monitored on the oscilloscope when applying 440 V over the GEM. The discharge was filmed with a digital camera and it showed that the GEM re-establishes its original potential levels as before the breakdown, though with a short delay due to the capacitors coupled between the GEM and ground, and then it continuous to operate properly after the breakdown. This was observed even though no protective resistors were restricting the current during the breakdown and further supports the fact that the GEM is a reliable and robust device. Discharges may propagate down to the readout board under certain circumstances, and if so happens, it could severely destroy the electronics [II]. Fortunately, it was found that the threshold for a propagation to occur, is at an electric field strength above 10 kV/cm, which is far more than the 1 kV/cm needed in the induction region [III].

Large currents were measured at the GEM electrodes when irradiated with low energy x-rays, up to 0.2 mA, see figure 7 in [I]. Even larger currents were obtained in the Racetrack tests, and no protective resistors was used. In this case individual HV supplies were connected to each GEM electrode, and they should manage to keep the potential stable during operation inspite of fast changes in the photon fluence rate. Maybe a capacitive coupling from the GEM to ground, as described in [IV], could be used in order to keep the potential stable and protect the GEM in case of a discharge, by delaying and even out the current.

To understand how the electrons and ions move inside the detector in a multilayer structure, the currents were measured at all electrodes in a triple GEM setup (one placed in CAT mode). The result is presented in [II]. Interesting was that if increasing the potential over the CAT, an increasing current was seen at the drift electrode, caused by an ion feedback (figure 4(b) in [II]). Such effects must be considered when analyzing the signal of a final multilayer detector.

Stability tests were made with low energy x-rays. Figure 8 in [I] for example, shows a signal variation of less than 0.4% when measured a second time five minutes later. The stability test performed during one hour showed a variation of less than 1%. The signal measured at different days for the same setup showed good agreement too. However, long stability tests remains to be done in the treatment accelerator.

A single GEM setup proved to have a linear response with the incident photon fluence rate at both diagnostic photon energies (50 kV spectrum), figure 7 in [IV], and at high treatment energies (50 MV spectrum), figure 10 in [IV]. The photon fluence rates were very high during the linearity tests, maximum $\sim 10^8$ photons $\text{mm}^{-2}\text{s}^{-1}$ for the x-ray tube, and $\sim 10^{10}$ photons $\text{mm}^{-2}\text{s}^{-1}$ during the pulses at the treatment accelerator. Especially note that the detector signal shows a very good correspondence with the accelerator current, measured during the short pulse length at the Racetrack. The pulse measurement was obtained in the same setting as described for figure 3.7. A linear response was also obtained for a double GEM setup for low energy x-rays (30 kV spectrum), figure 8 in [IV], and this indicates that no space charge is created between the GEM layers. The linearity to the photon fluence rate is a crucial parameter for an imaging detector, and it is therefore very positive results obtained here, considering the intended application of this detector.

Examples of low energy images obtained in a single GEM mode

Initial low energy images were achieved with 10 to 60 kV x-ray spectra. For simplicity high contrast objects were imaged at the beginning. Figures 3.8 A) and B) show a wrench made of stainless steel and a piece of Pb. The x-ray tube was operated at 40 kV and 15 mA, and the integration time was 1 s.

To exemplify a biological object with a less pronounced contrast, a 15 mm thick lamb chop was imaged, see figure 3.9 A). The best detail contrast was obtained with the x-ray tube set to 30 kV and 15 mA. A 0.5 mm Al filter was placed in front of the x-ray window to filter out low energy photons that do not contribute to the signal. The integration time was 1 s and the imaged object was placed immediately in front of the detector, while the detector was at a distance of 123 cm from the source. The image shows that the adipose tissue (fat) at the edges is distinguishable from the muscles, as is the bony structure. The central hole in the bone originates from the spinal cord. A photo of the object is shown for comparison in figure 3.9 B). The axes of the x-ray image are overlaid the photo, and the object as visualized in the x-ray image show good agreement with the photo.

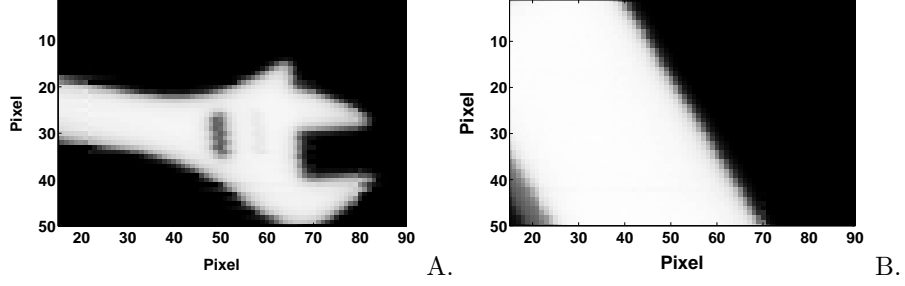


Figure 3.8: X-ray images of high contrast objects: A) shows a wrench and B) the edge of a piece of Pb. The x-ray tube was set to 40 kV.

When calculating the mean value of about 50 pixels, from the muscles area and the adipose area respectively, it was found that the measured contrast was 36% between the two types of tissues. The inherent contrast for this setting was expected to be 32%. Hence the contrast in the obtained image is rather close to the theoretical value.

The images presented in this thesis have not been subject to any advanced image processing, but a simple normalization only as to be described. All pads on the FEC are individually connected to the ASIC chip, and have thereby their own offset value defined by the electronics. By acquiring a dark field image (with no x-ray on), the corresponding matrix of individual pixel offset values, *Offset*, is obtained. The raw data acquired when irradiating the detector with a uniform x-ray beam, a so called 'flat field' image, is referred to as *Uniform*, and the raw data for a signal image, *Signal*, is the image acquired with an object in front of the detector when irradiating with the same settings as for the uniform image. The final image, *Image*, is obtained by normalizing the signal image to the flat field image according to

$$Image = \frac{Signal - Offset}{Uniform - Offset} \quad (3.1)$$

The normalization procedure creates areas corresponding to total photon absorption as white areas, and full radiation (no absorption) as black areas in the images. In some cases saturated pixels have been interpolated.

3.2.3 Double GEM + metal converter plate setup

Electron transmission through a converter plate

The electron transmission through the converter plate is of major importance for the detector function. In one test series a perforated stainless steel plate was mounted in chamber 1 with the purpose to measure the transmission. The

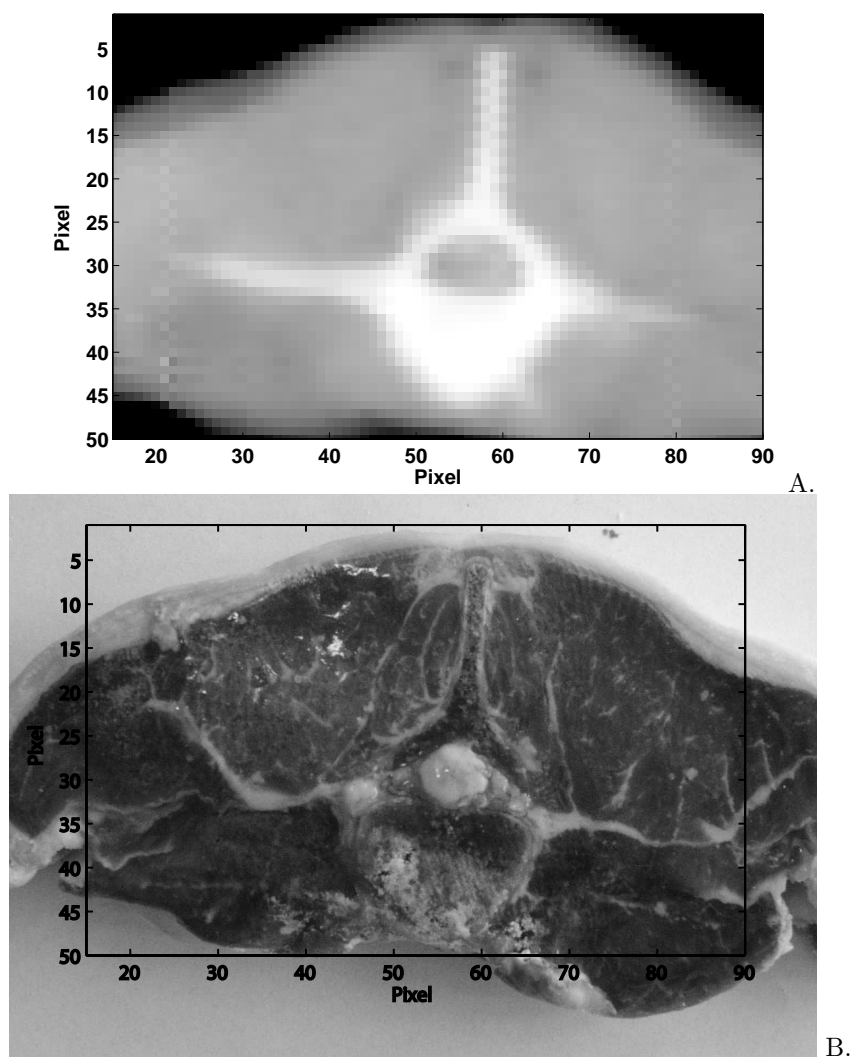


Figure 3.9: A) Image of a 15 mm thick lamb chop when irradiated with a 30 kV x-ray spectrum during 1 s integration time. B) Photo of the imaged lamb chop. The axes from the x-ray image has been transferred to the photo in order to make a comparison easier. The outline of the various structures in the object as seen in in the photo, such as fat, muscles and bone, are recognized at corresponding pixel value in the x-ray image.

0.15 mm thick plate was perforated in a quadratic pattern with holes ($\phi=0.3$ mm) at a pitch of 1.27 mm, hence the optical transparency was $\sim 4\%$ over an active area of $40 \text{ mm} \times 40 \text{ mm}$. However, as is presented in [II], the obtained electron transmission was very low, and therefore a new converter plate with a significantly higher optical transparency was constructed.

The new converter was a $100 \mu\text{m}$ thick Cu plate etched² with holes of $200 \mu\text{m}$ at a pitch of $280 \mu\text{m}$, and had an active area of $100 \text{ mm} \times 100 \text{ mm}$, see figure 3.10. The optical transparency was $T_{\text{optical}} \approx 46\%$. The converter was mounted (see figure 3.11) between two GEM foils in chamber 2 according to the setup illustrated in figure 3.12.

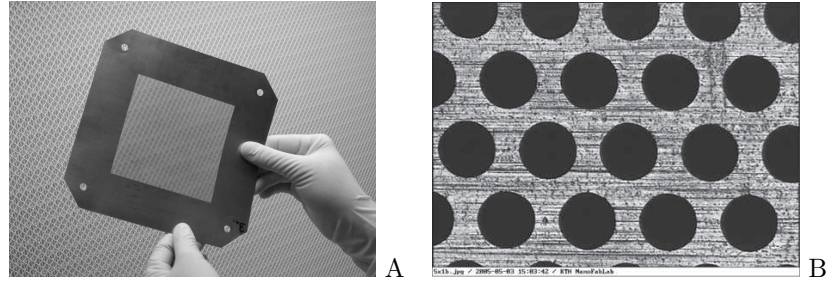


Figure 3.10: A) Photo of the Cu converter plate used during the tests. The $\sim 50\%$ transparency is clearly seen. B) Microscope photo of the same converter (the hole diameter is $200 \mu\text{m}$), Mårten Stjernström, KTH NanoFabLab.

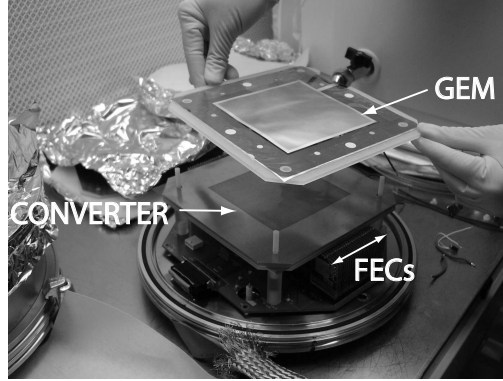


Figure 3.11: Installation of the Cu converter plate between two GEMs in chamber 2. A Cu mesh was used as drift electrode and the dedicated electronic readout system (FECs) was installed at the bottom of the chamber.

The transmission test was performed with constant 40 kV and 20 mA applied to the Philips tube. The potential drop over GEM1 (see figure 3.12) was varied in order to increase the number of electrons incident on the converter plate, so that the transmission could be measured at several electron fluence rates. The

²The chemically etching process was made by HP Etch AB in Stockholm.

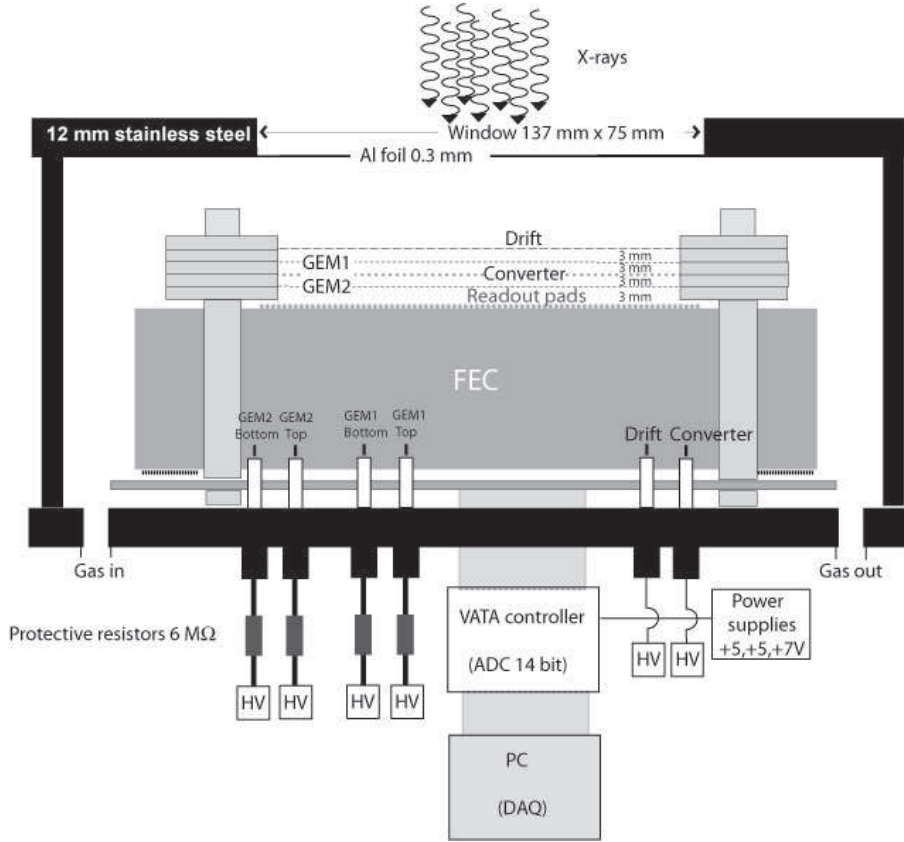


Figure 3.12: The test setup during the measurements of the electron transmission through the solid converter plate. X-ray images were also acquired for this setup.

same effect could have been achieved by increasing the incoming photon fluence rate (mA on the x-ray tube).

The electron transmission was calculated by dividing the current measured at GEM2 (transmitted electrons) with the incident current at the converter plate.

The current at the two layers was measured in separate test series with a Keithley 610C Solid state analogue Electrometer when increasing the voltage drop over GEM1. The electric field strength was constantly 1.33 kV/cm in the transfer 1 region above the converter. During the current measurement at the converter plate, the GEM2 electrodes were grounded so that all electric field lines ended at the converter plate and assuring that all electrons were collected here. When the fraction of electrons transmitted through the converter plate was measured at GEM2 (top and bottom electrodes in shortcut), the electric field strength in the transfer 2 region was set to two different values in order to see the transmission dependance of the field strength above and under the converter. The ionization chamber current generated by primary photons in the transfer 2 region was

subtracted from the measured value.

The average electron transmission was found to be 13.6% when the electric field strength was the same above as below the converter plate. For the increased field strength below the converter, an average electron transmission of 15.4% was achieved according to figure 3.13.

Hence, for this dimension of the converter plate the electron transmission is approximately one third of the optical transparency. The transmission could possibly be larger if increasing the field strength below the converter further. Anyhow, the multiplication in the GEM can be set to a comparatively low value to compensate for the absorption losses in a converter plate of the given dimensions.

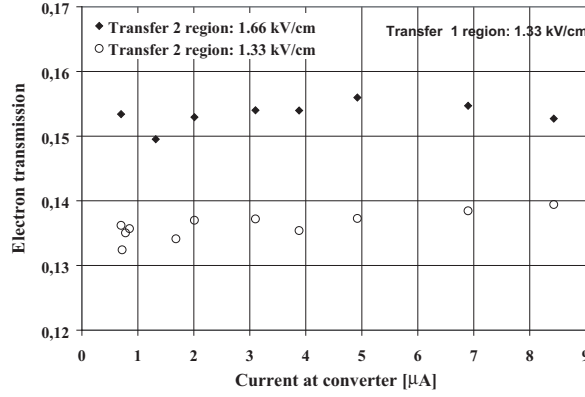


Figure 3.13: Electron transmission through a Cu converter plate of thickness $100 \mu\text{m}$ and an optical transparency of $T_{\text{optical}} \approx 46\%$. A higher transmission is achieved when the electrical field strength below the converter (Transfer 2 region) is higher than above it (Transfer 1 region).

Images acquired with the converter plate installed

In parallel with the electron transmission test, objects were imaged. For example was a metallic screw and a nylon screw taped to a 5 mm thick slab of PMMA (see photo in figure 3.14 B) and imaged with 40 kV spectrum and a 0.5 mm Al filter. The image is shown in figure 3.14 A). The nylon screw is visible in the image even though there is only a small contrast difference between the screw and the PMMA plate. The metallic screw is clearly seen as expected, but even the very thin insulating tape is vaguely visible. The dark lines are due to a saturated signal in some pixels in the uniform image that is used for the normalization.

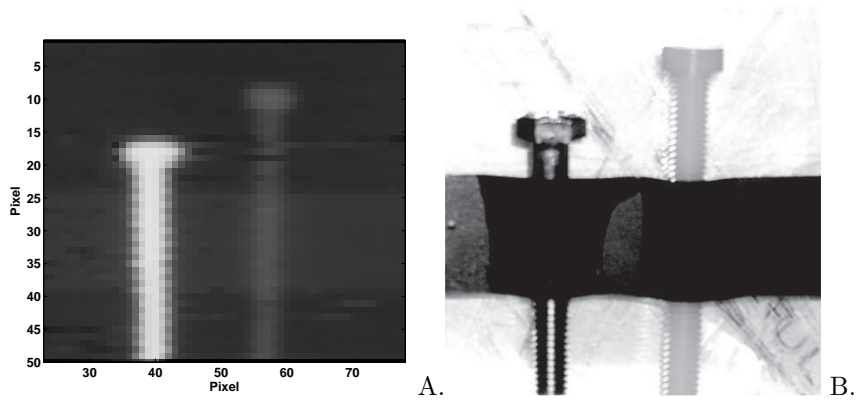


Figure 3.14: A) X-ray image of a metallic screw and a nylon screw attached to a 5 mm PMMA slab with insulating tape. B) Photo of the imaged objects.

Chapter 4

Discussion and conclusions

4.1 Potential clinical applications

Portal Imaging The new detector is envisaged to have a capability of acquiring high-quality portal images at a high rate. This is enabled by the following features, a high quantum efficiency to obtain the required SNR in a short time, and a fast readout system. The readout allows to capture digital images of the treatment port in real time (200 fps and higher) throughout the fraction, i.e. the detector would be able to monitor each single pulse if the pulse rate is 200 Hz or lower. Radio opaque markers are increasingly used to locate the target volume and could be traced in real time. With the outlined verification capability, the quality of patient treatments may be increased by real time adaptive radiation beam alignment on the target with on-line corrections during each treatment fraction. Alternatively an adaptive radiation treatment where the recorded treatment deviations are considered for correction during the following treatment sessions.

Computed Tomography The large detector area and high data acquisition speed allow for a cone beam CT reconstruction within the treatment room. The dual energy function of the detector actually allows both MVCT and kVCT imaging. About 800 projections are needed for a CT reconstruction if assuming 400×500 pixels. With a readout speed of 200 fps all data for a 3D volume of the patient could theoretically be generated in less than 5 seconds. The rotation speed of the gantry may be a limiting factor. Usually the accelerators make maximum one revolution per minute¹. A slower scan will increase the signal to noise ratio since more data will be acquired in every angle, but will also increase the risk for motion blurring. Modern CT scanners makes as many as 3 revolutions per second.

¹Standards for Accelerators (IEC) generally recommend the rotation of the gantry to be up to 1 rpm [48].

Use of CT technology further enables identification and the exact location of the target in 3 dimensions immediately prior the treatment. Inter-fractional (between the treatment sessions) tumor motion is common and with the patient in a position ready for the treatment, the target displacements can be accounted for. If the nearby critical organs are localized, and combined with information concerning the exact target position, one can not only minimize the risk of irradiating healthy tissue but also escalate the dose to the target volume.

Separate simulators or virtual simulators (CT with simulation software) outside the treatment room might be superfluous if introducing this imaging device, since simulation images could be achieved with the patient laying in the right position on the real treatment couch.

Practical constraints in clinical applications To implement diagnostic quality imaging with the detector, an x-ray tube can be added to the gantry in the treatment room, see figures 4.1 and 4.2. The detector may be gantry-mounted on a robotic arm which can be remotely controlled. Images can be acquired at all gantry angles. The detector unit should be fully retractable. The optimal solution would be to include the kV-tube inside the gantry head, then the treatment beam and diagnostic beam may be perfectly aligned. Such a solution is more complicated though since it must be fully integrated with the accelerator.

To optimize the detector function for the diagnostic and the therapeutic operations, two modes of internal settings may be defined. This may include a switch of the high voltage potential to maximize the image quality. If it is feasible to switch modes fast enough the kV beam could run continuously during the treatment and radiographs would then be acquired between the pulses from the accelerator beam, and in that way keep a real time intra-fractional tumor tracking, i.e. dynamic imaging.

4.2 Summary of the experimental work

Numerous measurements have been performed with various GEM setups verified. For a single GEM setup a linear response with the photon fluence rate at both diagnostic photon energies (10-50 kV spectrum) and at high treatment energies (50 MV spectrum) was measured. The photon fluence rates were very high, maximum $\sim 10^8$ photons $\text{mm}^{-2}\text{s}^{-1}$ for the x-ray tube and $\sim 10^{10}$ photons $\text{mm}^{-2}\text{s}^{-1}$ during the pulses at the treatment accelerator. A linear response was also obtained in a double GEM setup for low energy x-rays and this indicates that no space charge is created between the GEM layers. The linearity to the photon fluence rate is an important parameter for an imaging detector in order not to have to impose rate dependent correction factors and avoid saturation effects.

The GEM multiplication was operating normally in the high energy and high

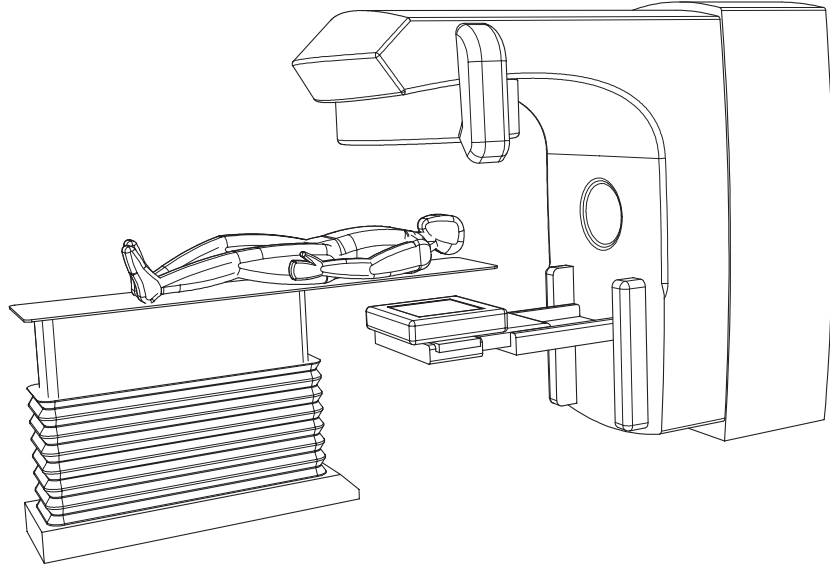


Figure 4.1: During the treatment the EPID is placed opposite the gantry head for a real time imaging mode.

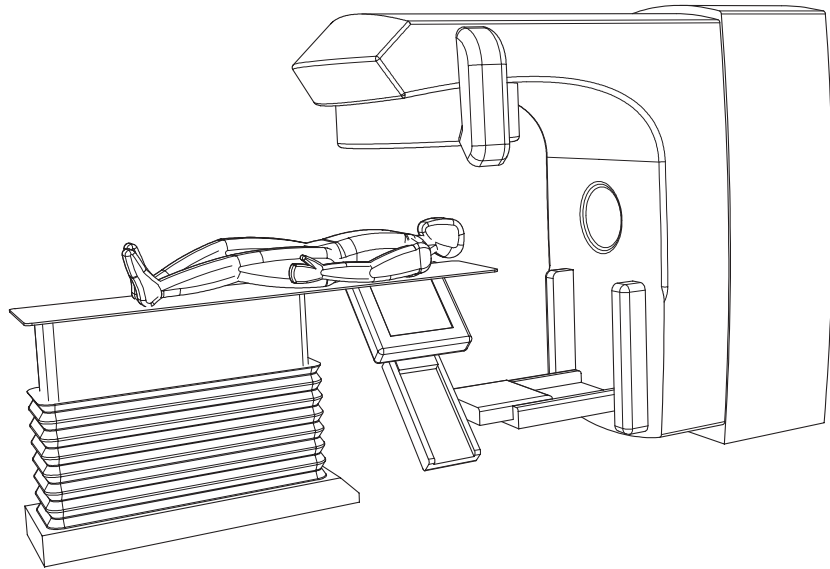


Figure 4.2: An additional x-ray source could be attached to the gantry head as shown in the figure. The detector must then be tilted correspondingly in order to be aligned with the beam of the x-ray tube during the collection of the CT data.

fluence rate treatment beam where a maximum gain of 100 was achieved. This is rather low compared to gains in the order of 10^4 that can be obtained in a less harsh environment. However, the gain needs only to be high enough to compensate for the absorption losses in the converter plates. According to the electron transmission measurements, around a factor 10 would be sufficient in our application.

The concept of the new electronic readout system has proven to be robust and reliable and capable of acquiring images at diagnostic energies. The imaging acquisition speed has been verified with e.g. tracks from alpha particles imaged in real time with a speed of 188 fps.

4.3 Future developments

With the aim of constructing an optimal working portal imaging device, useful in the clinical routine at radiation treatment departments over the world, there are several features to be considered.

Monte Carlo simulations must be carried out to find the optimal configuration of the detector in order to acquire the best information for the CT and portal images. For example the total number of layers, the layer inter-distances, the gas mixture, the converter geometry and material, the level of multiplication in the GEMs, electrical field strengths in the drift, transfer and induction region needs to be optimized. In parallel the expected performance must be verified experimentally in a real treatment beam.

To achieve better kV CT images it would be useful to come up with an idea of how to combine the drift electrode with an efficient converter for low energy photons with a higher QE compared to the gas layer [IV].

By combining the converter plate and the GEM to one device, i.e. constructing GEM foils with a thick bottom electrode for example, the total thickness of the detector can be reduced. A thin detector volume will minimize the parallax error and also reduce the high voltage potentials applied. The electron transmission of such a device should be improved compared to the converter plate described in this thesis.

In the strive to develop a useful portal imaging device to be implemented in a clinical environment, it should be analyzed and tested whether a recirculating sealed system could be used or not. This would simplify the installation and daily running of the detector system in a clinical application.

A feature not discussed in this work would be to use the device for portal imaging dose estimations. This should be analyzed and tested.

4.4 Concluding advantages and challenges with the new detector

The main potential advantages of the system can be summarized as:

- Wide and adjustable energy range
⇒ THREE MODES OF PROJECTED OR TOMOGRAPHIC IMAGING:
 1. kV DIAGNOSTIC IMAGING
 2. MV THERAPEUTIC IMAGING
 3. DIAGNOSTIC AND THERAPEUTIC IMAGING WITH THE SAME DEVICE
- Multilayer structure with several converter plates
⇒ HIGH EFFICIENCY FOR PORTAL IMAGING
- Highly radiation resistant since only radiation resistant materials are used and all electronics are placed outside the radiation beam and can be retracted
⇒ LONG OPERATIONAL LIFE TIME
- Fast data acquisition, at least 200 fps with the prototype detector
⇒ CT & FAST REAL TIME ADAPTIVE IMAGING
- High quantum efficiency with the multilayer structure gives higher sensitivity, less noise and makes the faster response possible
⇒ ENHANCED IMAGE QUALITY
- Possible to manufacture large area detectors
⇒ LARGE ACTIVE AREA, 40 CM × 50 CM AND BEYOND

The major challenges with the new detector:

- Gas supply needed
⇒ IN CASE OF A NON SEALED SYSTEM GAS REFILL AND CIRCULATION REQUIRED
- Relatively large pixel size with present readout system
⇒ SPATIAL RESOLUTION COMPARABLE TO EXISTING EPID SYSTEMS
- Increased thickness of multilayer detector compared to AMFPI's
⇒ SPATIAL RESOLUTION LIMITED BY PARALLAX ERROR AT THE EDGES FOR THICK DETECTORS
- High voltage required
⇒ PROPER HV INSULATION REQUIRED
- Mechanical design more complicated
⇒ APPROPRIATE MECHANICAL ENGINEERING REQUIRED

Acknowledgements

Primary gratitude goes to my supervisors Mats Danielsson and Anders Brahme for giving me the opportunity to work in such a interesting project, and who's help and knowledge has been invaluable during the writing. I owe Vladimir Peskov and Christian Iacobaeus many thanks for their guidance and expertise in the experimental work that we made together during the many GEM measurements. Further was the floating HV-supplies built by Christian. I would also like to acknowledge the contribution of Monika Ågren (former Wallmark) and Andreas Rundström during their diploma work within the project. The results based on the Monte Carlo simulations (section 2.2) were an important part of the thesis I think, and I certainly appreciate the work of Nial Wassdahl who ran all the simulations for me. Other contributions included in this thesis are the figures 4.1-4.2, that were provided by Fred Persson, and also the photon fluence rate for the Philips x-ray tube (figure 3.1) that was kindly measured by Erik Fredenberg. Thanks all for your contribution to the work presented in this thesis.

Efficient is an appropriate word to use when describing the work performed by Roffe and his colleagues at the Albanova Mechanical Workshop when constructing various detector parts. I would also like to thank Stefan Rydström for his construction of the radiation protection in the laboratory, and not to forget, the detector stand, it has reduced the consumption of insulating tape and the use of phone books as detector support noticeably. Bengt Lind and Peder Näfstadius have operated the Racetrack at late evenings during the high energy measurements, thank you for your help. A person that I really appreciate is Bo Nilsson, not only for the valuable comments and discussions that he has provided, but also for his support during my years as a PhD student.

To all 'PAPERS' working in the Particle and Astroparticle Physics group at KTH, you have all contributed to a great working atmosphere (including a few parties now and then...) and I have really enjoyed your company. A special THANK YOU goes to Sara Bergenius Gayler: 1. How boring wouldn't a working day be without her? 2. Could I have finished this thesis without her endless encouragement? At the Medical Radiation Physics department I would like to thank Lil Engström and Ann-Charlotte Ekelöf for their help and support over the years.

(Answer: 1. Very 2. No)

Erik Hedlund has given me an invaluable understanding of the radiation therapy market during our work to establish the company **■C-RAD**, of which I have been employed one year now. Since the day Gunnar Norberg was employed in the company, him and I have had many discussions about the detector, and I'm glad for his patience in explaining electronics to me. I'm also grateful for the encouragement from my other colleagues, finally I will concentrate on doing some 'real' work with you...

Rötter i form av en familj är väldigt viktiga för att kunna uppnå det man vill och för mig betyder Mamma, Pappa, Mikael och Thorbjörn enormt mycket. Tjocka släkten, där rotsystemet utvidgat sig till Örebrofolket också, är det alltid full fart på och jag tycker om att umgås med er allihopa. Kul att så många ville vara med och fira! Det har inte funnits mycket tid till att träffa mina kompisar - men just eftersom ni är så bra kompisar så vet jag att ni finns kvar där ändå och det är jag väldigt glad för!

Jag kan inte tacka dig nog Peter J, ditt enorma stöd går som en röd tråd genom allt mitt arbete och dig tycker jag om mest av alla. P.K.K.P.

The work in this thesis has been supported by VINNOVA, the Particle and Astroparticle Physics group at the Royal Institute of Technology and **■C-RAD** Imaging AB.



There is a Jungle-saying 'When the Phantom moves, the lightning stands still'. If that is true, this must be the ultimate proof of how fast the detector imaging rate is, since he was captured on an image².

²Test setup: Double GEM + Converter, X-ray: 40 kV, 20 mA, 0.5 mm Al filter, SDD=130 cm, Kr-CO₂(90-10). The object is etched in 35 μ m Cu on a 1.6 mm PCB

Abbreviations

ADC - Analog to Digital Converter

AMFPI - Active Matrix Flat Panel Imager

ASIC - Application Specific Integrated Circuit

CAT - Compteur a Trou (hole counter)

CT - Computed Tomography

EPID - Electronic Portal Imaging Device

FEC - Front End Card

fps - frames per second

GEM - Gas Electron Multiplier

IMRT - Intensity Modulated Radiation Therapy

kV - Accelerating potential in kilovolt

keV - Energy in kilo electron Volt

MV - Accelerating potential in megavolt

MeV - Energy in Mega electron Volt

PMMA - Polymethyl Methacrylate

QE - Quantum Efficiency

rps - revolutions per second

SDD - Source to Detector Distance

SNR - Signal to Noise Ratio

Bibliography

- [1] M.Wallmark, A.Brahme, M.Danielsson, P.Fonte, C.Iacobaeus, V.Peskov, J.Östling, "Operating range of a gas electron multiplier for portal imaging", Nucl. Instr. and Meth. in Physics Research A 471 (2001) 151-155
- [2] V.Peskov, P.Fonte, M.Danielsson, C.Iacobaeus, J.Ostling, M.Wallmark, "The study and optimization of new micropattern gaseous detectors for high rate applications", IEEE T NUCL SCI 48 (4): 1070-1074 Part 1 AUG 2001
- [3] C.Iacobaeus, M.Danielsson, P.Fonte, T.Francke, J.Ostling, V.Peskov, "Sporadic electron jets from cathodes - the main breakdown-triggering mechanism in gaseous detectors", IEEE T NUCL SCI 49 (4): 1622-1628 Part 1 AUG 2002
- [4] C. Iacobaeus, M. Danielsson, T. Francke, J. Ostling and V. Peskov, "Study of capillary-based gaseous detectors", IEEE T NUCL SCI 51 (3): Part 1 JUNE 2004
- [5] M. Danielsson, P. Fonte, T. Francke, C. Iacobaeus, J. Ostling and V. Peskov, "Novel gaseous detectors for medical imaging", Nucl. Instr. and Meth. in Physics Research A 518 (2004) 406-410
- [6] C. Iacobaeus, P. Fonte, T. Francke, J. Ostling, V. Peskov, J. Rantanen, and I. Rodionov, "The development and study of high-position resolution (50 ?m) RPCs for imaging X-rays and UV photons", Nucl. Instr. and Meth. in Physics Research A 513 (2003) 244-249
- [7] C. Iacobaeus, A. Breskin, M. Danielsson, T. Francke, D. Mörmann, J. Ostling and V. Peskov, "Advances in capillary-based gaseous UV imaging detectors", Nucl. Instr. and Meth. in Physics Research A 525 (2004) 42-48
- [8] P. Aaltonen et. al., "Specification of dose delivery in radiation therapy - Recommendations by the Nordic Association of Clinical Physics (NACP)", Acta Oncol. 1997; 36 (suppl. 10): 1-32
- [9] J. Löf, B. K. Lind and A. Brahme, "An adaptive control algorithm for optimization of intensity modulated radiotherapy considering uncertainties in beam profiles, patient setup, and internal organ motion", Phys Med Biol 43, (1998) 1605-1628

- [10] L. E. Antonuk, "Electronical portal imaging devices: a review and historical perspective of contemporary technologies and research", *Phys. Med. Biol.* 47 (2002) R31-R65
- [11] M. G. Herman et. al., "Clinical use of electronic portal imaging: Report of AAPM Radiation Therapy Committee Task Group 58", *Med. Phys.* 28 (5), May 2001
- [12] J. Chang, G. S. Mageras, C. C. Ling, "Evaluation of rapid dose map acquisition of a scanning liquid-filled ionization chamber electronic portal imaging device", *Int. J. Radiation Oncology Biol. Phys.*, Vol. 55, No. 5, (2003) 1432-1445
- [13] M. Strandqvist, B. Rosengren, "Television-controlled pendulum therapy", *Br. J. Radiol.*, Vol. 31, (1958) 513-4
- [14] ELIAV, Medical Imaging Systems P.O. Box 10403, Haifa 26115, Israel, <http://www.eliaiv.com/>
- [15] Cablon Medicals, Klepelhoek 11, 3833 GZ Leusden, The Netherlands, <http://www.cablon.net/>
- [16] A. Sawant et. al., "Segmented crystalline scintillators: An initial investigation of high quantum efficiency detectors for megavoltage x-ray imaging", *Med. Phys.* 32 (10) October 2005
- [17] Perkin Elmer, 45 William Street, Wellesley, MA 02481-4078, USA, <http://www.perkinelmer.com/>
- [18] Elekta AB, Box 7593, SE-103 93 Stockholm, SWEDEN, <http://www.elekta.com/>
- [19] Siemens AG, Wittelsbacherplatz 2, D-80333 Munich, Federal Republic of Germany, <http://www.siemens.com/>
- [20] A. Del Guerra, "Ionizing Radiation Detectors for Medical Imaging", World Scientific Publishing Co. Pte. Ltd., Singapore 2004, ISBN 981-238-674-2
- [21] R. I. Berbeco, S. B. Jiang, G. C. Sharp, G. T. Y. Chen, H. Mostafavi and H. Shirato, "Integrated radiotherapy imaging system (IRIS): design considerations of tumour tracking with linac gantry-mounted diagnostic x-ray systems with flat panel detectors", *Phys. Med. Biol.* 49 (2004) 243-255
- [22] Varian Medical Systems, 3100 Hansen Way, Palo Alto, CA 94304, USA, <http://www.varian.com/>
- [23] L. J. Forrest et. al., "The utility of megavoltage computed tomography images from a helical tomotherapy system for setup verification purposes", *Int. J. Radiation Oncology Biol. Phys.*, Vol. 60, No. 5, (2004) 1639-1644
- [24] A. Brahme, B. Lind and P. Näfstadius, "Radiotherapeutic computed tomography with scanned photon beams", *Int. J. Rad. Oncol. Biol. Phys.* 13: 95 (1987)

- [25] A. Brahme, M. Danielsson, patent No. US 6,429,578 (B1) "Diagnostic and therapeutic detector system for imaging with low and high energy x-ray and electrons", (2002)
- [26] F. Sauli, "GEM: A new concept for electron amplification in gas detectors", Nucl.Instr.Meth.A 386 (1997) 531-534
- [27] <http://ts-dep-dem.web.cern.ch/ts-dep-dem/products/gem/geminfo.htm>
- [28] <http://ts-dep-dem.web.cern.ch/ts-dep-dem/products/gem/welcome.htm>
- [29] Flyer aquired from the CERN Transfer Technology website via the webaddress <https://oraweb.cern.ch/pls/ttdatabase/display.main>
- [30] Reprinted from Nuclear Instruments and Methods in Physics Research Section A, 471, S. Bachmann, A. Bressan, S. Kappler, B. Ketzer, M. Deutel, L. Ropelewski, F. Sauli, E. Schulte, "Development and applications of the gas electron multiplier", 115-119, Copyright (2005), with permission from Elsevier
- [31] S.Bachmann, A. Bressan, A.Placci, L. Ropelewski and F. Sauli, "Development and Test of Large Size GEM Detectors", IEEE T NUCL SCI 47 (4): 1412-1415 AUG 2000
- [32] F. Bartol, M. Bordessoule, G. Chaplier, M. Lemonnier, S. Megtert, "The C.A.T. pixel proportional gas counter detector", J.Phys. III France 6 (1996) 337-347
- [33] W. R. Leo, "Techniques for nuclear and particle physics experiments", 2nd ed., Springer-Verlag, Germany (1994), ISBN 0-387-57280-5
- [34] D. W. Anderson, "Absorption of Ionizing Radiation", University Park Press, Baltimore, USA
- [35] R. Kihlberg, Hestra Elektronik Swe AB, Öreryd, S-330 27 HESTRA, Sweden
- [36] Gamma Medica -Ideas, Inc., www.gammamedica.com, Oslo, Norway
- [37] A. Brahme, C. Iacobaeus, R. Kihlberg, J. Oestling, patent No. US 6,841,784 (B2) "Radiation sensor device", (2005)
- [38] F. Salvat, J.M Fernandez-Varea and J. Sempau, "PENELOPE - A Code System for Monte Carlo Simulation of Electron and Photon Transport", OECD Nuclear Energy Agency, Issy-les-Moulineaux, France, 2003
- [39] G. X. Ding, "Energy spectra, angular spread, fluence profiles and dose distributions of 6 and 18 MV photon beams: results of MOnTe Carlo simulations for a Varian 2100EX accelerator", Phys. Med. Biol. 47 (2002) 1025-1046
- [40] M. A. Duch, "Desarrollo de Tcnicas Dosimtricas para su Aplicacin en Dosimetra "in vivo" en Terapia de Alta Energia", PhD Thesis, Universitat Politcnica de Catalunya, Barcelona (1998)

- [41] "estar: Stopping power and range tables for electrons", <http://physics.nist.gov/PhysRefData/Star/Text/ESTAR.html>, Physics Laboratory, National Insitute of Standards and Technology (NIST), USA
- [42] T. Tabata, R. Ito, S. Okabe, "Generalized Semiempirical Equations for the Extrapolated Range of Electrons", Nucl.Instr.Meth.A 103 (1972) 85-91
- [43] B. Nilsson, A. Brahme, "Contamination of high energy photon beams by scattered photons", Strahlentherapie 157: 181 (1981)
- [44] J. H. Hubbell, S. M. Seltzer, "Tables of x-ray mass attenuation coefficients and mass energy absorption coefficients for 1 keV to 20 MeV for elements Z=1 to 92 and 48 additional substances of dosimetric interest", NISTIR 5632, NIST (1995)
- [45] R. Birch, M. Marshall and G.M. Ardran, "Catalogue of spectral data for diagnostic X-rays", Scientific Report Series 30, The Hospital Physicists' Association, London (1979)
- [46] A. Brahme, H. Svensson, "Radiation beam characteristics of a 22 MeV microtron", Acta Radiol. 18: 244 (1979)
- [47] A. Cardini, "A systematic study on discharge-induced GEM-failure phenomena", IEEE Nuclear Science Symposium Conference Record, N26-7, (2005)
- [48] International Electrtechnical Comission (IEC), "Safety of medical electrical equipment - Part 1 General requirements", Publ. 601-1 IEC, Geneva (1981)